One-pot prepared mesoporous silica SBA-15-like monoliths with embedded Ni particles as selective and stable catalysts for methane dry reforming

Oscar Daoura, Giulia Fornasieri, Maya Boutros, Nissrine El Hassan, Patricia Beaunier, Cyril Thomas, Mohamed Selmane, Antoine Miche, Capucine Sassoye, Ovidiu Ersen, et al.

One-pot prepared mesoporous silica SBA-15-like monoliths with embedded Ni particles as selective and stable catalysts for methane dry reforming

Oscar Daoura[a,b], Giulia Fornasieri[c], Maya Boutros[a], Nissrine El Hassan[d], Patricia Beaunier[b], Cyril Thomas[b], Mohamed Selmane[e], Antoine Miche[b], Capucine Sassoye[f], Ovidiu Ersen[g], Walid Baaziz[g], Pascale Massiani[b], Anne Bleuzen[c]* and Franck Launay[b]*

[a] Laboratoire de Chimie Physique des Matériaux (LCPM/PR2N), Lebanese University, Faculté des Sciences II, Campus Fanar, BP 90696 Jdeideh, Lebanon.

[b] Laboratoire de Réactivité de Surface (LRS), UMR 7197 CNRS - Sorbonne Université, Campus Pierre et Marie Curie, 4 place Jussieu, F-75005 Paris, France. franck.launay@sorbonne-universite.fr

[c] Institut de Chimie Moléculaire et des Matériaux d'Orsay (ICMMO), UMR 8182 CNRS - Université Paris-Saclay, F-91405 Orsay, France. anne.bleuzen@u-psud.fr

[d] University of Balamand, Department of Chemical Engineering, P.O. box 33, Amioun El Koura, Lebanon.

[e] Institut des Matériaux de Paris Centre (IMPC), FR 2482 CNRS - Sorbonne Université, Campus Pierre et Marie Curie, 4 place Jussieu, F-75005 Paris, France

[f] Laboratoire de Chimie de la Matière Condensée de Paris (LCMCP), UMR 7574 CNRS - Sorbonne Université, Campus Pierre et Marie Curie, 4 place Jussieu, F-75005 Paris, France.

[g] Institut de Physique et de Chimie des Matériaux de Strasbourg (IPCMS), UMR 7504 CNRS - Université de Strasbourg, 23 rue de Loess, BP43, 67034 Strasbourg Cedex 2, France.

Abstract:

Ni@SBA-15 monoliths with up to 5 wt.% of Ni were successfully synthetized by means of an original and easy one-pot sol-gel method. Transmission Electron Microscopy (TEM), X-ray Photoelectron Spectroscopy (XPS), Temperature-Programmed Reduction (TPR), Pair Distribution Function (PDF) and X-Ray Diffraction (XRD) were used for the structural characterization of the samples. After H_2-reduction, those solids exhibited small Ni^0 particles (between 1-3 nm) highly dispersed (one of the highest dispersion reported in the literature to date for 5 wt.%

Ni/Silica materials) in strong interaction with the silica support. Scanning Transmission Electron Microscopy in the High Angle Annular Dark Field (STEM/HAADF) mode, chemical mapping by Energy Dispersive X-Ray (EDX) spectroscopy and electron tomography in STEM-HAADF mode highlighted the presence of Ni particles homogeneously distributed, especially in the mesopores. Such confined Ni nanoparticles were shown to be very selective and stable in the dry reforming of methane.

I. Introduction

Due to their reasonable activity and low cost, Ni-based catalysts are preferred to noble metals-based ones in the Dry Reforming of Methane (DRM) reaction [1]. However, these catalysts undergo rapid deactivation, due to Ni oxidation (by surface adsorbed oxygen species during the catalytic process) [2], particle sintering [3] and coke formation [4]. The DRM reaction, which converts two major greenhouse gases into a useful chemical feedstock [5], is highly endothermic (high temperatures are therefore needed in order to achieve acceptable conversions) and is accompanied by different side reactions such as CH_4 decomposition ($CH_{4(g)} = C_{(s)} + 2\ H_{2(g)}$) and the Boudouard reaction ($2\ CO_{(g)} = C_{(s)} + CO_{2(g)}$) [6], which are responsible for carbon deposition. To avoid coke formation, well-dispersed small nickel particles [7] confined in the mesoporosity of an oxide support [8] and in strong interaction with it [9] have been claimed to be very suitable candidates to provide efficient and stable DRM catalysts [10]. Silica-based supports characterized by high specific surface areas, tunable pore sizes and the confined space provided by their porosity and the presence of silanol groups are ideal candidates. Despite the numerous investigations performed in this field to date, the preparation of such catalysts is still challenging [11]. In fact, the majority of the Ni-silica catalysts with relatively good catalytic performance were prepared by complicated and/or even expensive pathways such as those based on (i) original nickel precursors [12], (ii) ligands and complexing agents [13], (iii) sophisticated supports [14] or (iv) promoters and bi-metallics [15, 16]. Confining metal particles within the pores of a mesoporous support [17] or in capsules made of a mesoporous material [14,18] is a common method to control their dispersion and to protect them from sintering by using a physical barrier especially if the metal particles are anchored in the oxide support itself [18]. In particular, mesoporous SiO_2 and

ordered SBA-15 materials appear as very attractive owing to their unique textural properties. These solids, widely studied for nickel dispersion, give rise to promising catalysts [17,19]. Ni/SBA-15 silica catalysts are commonly prepared through post-synthesis impregnation of the silica support with an aqueous nickel solution. Even at relatively low Ni contents (around 5 wt.%) and despite the various syntheses modes used, part of the nickel particles are found to be deposited on the external surface of the silica grains, which makes them weakly stabilized by the oxide carrier. Therefore, Ni sintering may readily take place if the drying step following impregnation and / or the activation step are carried out under rather severe conditions [20]. The one-pot preparation method appears to be an attractive alternative to overcome the above-mentioned limitations. However, the preparation of Ni-silica catalysts using this method is not straightforward due to the difficult formation of Ni-O-Si bonds under the strongly acidic conditions required for the synthesis of these silica-based materials [21]. Under strongly acidic conditions, the silanol groups are protonated ($Si\text{-}OH_2^+$) and the resulting positively-charged oxide surface hardly interacts with cations such as Ni^{2+} [22]. A pH adjustment strategy (consisting in the controlled increase of the pH of the synthesis gel during the hydrothermal treatment) may be helpful for the nickel incorporation but may likely be detrimental for the textural properties of the resulting materials [23, 24].

This present contribution aims at reporting on the design of small Ni^0 nanoparticles (NPs) well dispersed onto ordered mesoporous SBA-15-silica monoliths by using a relatively easy and original one-pot sol-gel method [25]. This method is based on the rapid gelation of a mixture of a structure-directing agent (Pluronic P123), a silica source (tetramethylorthosilicate, TMOS) and an acidic aqueous solution of the nickel precursor. The monolithic carriers, whose shape can be customized, facilitate heat and mass transfers and afford attractive pressure drop properties, compared to powder catalysts [26]. In our study, SBA-15-silica monoliths with 2.5 to 5.0 wt.% of Ni, were prepared. Their textural properties, Ni NPs distribution, size and oxidation state as well as the Ni-support interaction were studied by N_2 sorption, classical TEM, STEM/HAADF, electron tomography, EDX/mapping, H_2 chemisorption measurements, PDF, XPS and H_2-TPR. For the sake of comparison, two additional materials containing 2.5 and 5.0 wt.% Ni were also prepared through the impregnation of a SBA-15 monolith using the "Two-Solvents" (TS) method [27]. Among the

prepared catalysts, the one synthesized using the one-pot method with 5.0 wt.% Ni seems to be very promising for the DRM reaction. Owing to its preparation method and obtained properties, such a solid appears as very interesting from an industrial point of view.

II. Experimental part

II.1 Materials preparation

The mesostructured silica monoliths were synthesized using tetramethylorthosilicate (TMOS) as a silica source and an amphiphilic block copolymer poly(ethylene glycol)$_{70}$-block-poly(propylene glycol)$_{20}$-block-poly(ethylene glycol)$_{70}$ (Pluronic P123, 5800 g mol^{-1}) as a structure-directing agent. For a typical synthesis of the SBA-15 monolith (denoted S), 2.4 g of P123 were added to 4 g of TMOS in a 30 mL poly-propylene vial and the solution was stirred in a water bath at 50°C until the polymer had been completely dissolved. After cooling to R.T., 2 mL of an aqueous acidic solution (HNO_3/H_2O pH = 1.3) were quickly added to the stirred TMOS-P123 clear mixture. The resulting solution was divided into four vials, which were closed tightly and transferred in a thermostated water bath at 23 °C to be aged overnight without stirring. After removing the vial lid, the resulting viscous sol gelled within 6 h giving a translucent gel. The ageing process was continued for one week in order to obtain homogeneous white glassy silica–copolymer monoliths. Finally, the solid was calcined in three steps (from R.T. to 100°C in 1 h followed by 1 h at 100°C, then from 100°C to 250°C in 8 h followed by 2 h at 250°C and from 250°C to 500°C in 8 h followed by 4 h at 500°C; Fig. S1), in order to optimize the removal of water, of the structure-directing agent and, last but not least, favor the densification of the silica framework.

For one-pot syntheses, a similar protocol was used. An adequate quantity of $Ni(NO_3)_2.6H_2O$ (197.5 or 395.0 mg corresponding to 2.5 ($Ni^{II}_{2.5\%}$@S) or 5.0 ($Ni^{II}_{5\%}$@S) wt.% of Ni, respectively) was dissolved in the aqueous acidic solution before mixing with the P123-TMOS mixture.

For a comparison purpose, two reference materials, $Ni^{II}_{2.5\%}$/S and $Ni^{II}_{5\%}$/S, were prepared by the “Two-Solvents” (TS) method. In that case, 250 mg of the S monolith

were suspended in *n*-heptane (with an appropriate volume to cover the solid) for a couple of minutes. A volume of water slightly lower than that of the silica pore volume (as previously determined by N_2 sorption) and containing an appropriate amount of nickel precursor was added dropwise. Due to the differences in polarity of *n*-heptane and water, the aqueous solution enters the porosity of the SBA-15 monolith, leading to the confinement of nickel. The solid was then removed from *n*-heptane, dried at RT and finally calcined, under static air, at 550 °C for 6 h (heating rate 1°C min^{-1}).

II.2 Solid characterizations

Textural properties were determined from N_2 adsorption-desorption isotherms recorded either on a Belsorp-max (BEL JAPAN) or ASAP 2020 (Micromeritics) apparatus. Before measurements, the samples were degassed under vacuum for 2 h at 250°C either on a BelprepII-vac unit or the ASAP 2020 equipment. Specific surface areas were obtained by using the BET equation. Pore diameters and specific pore volumes were determined using the BJH model. The textural properties were calculated by taking into account the siliceous support weight only (without Nickel).

Low and wide angles XRD measurements were performed either on a Brüker D8 Advance diffractometer or an X'Pert3 Powder diffractometer (PANalytical, Netherlands) with CuKα radiation sources (1.54 Å) operating at 30 KV and 10 mA. Low and wide angles data were recorded in the 2 theta range between 0.5 and 5°, and 5 and 90° with a step size of 0.01° and 1 s per step. The mean nickel/nickel oxide particles size was calculated from the Scherrer equation: $D = K\lambda/\beta\cos\theta$, where K is a constant (K=0.9), λ is the wavelength of the radiation source (1.54 Å), β is the full width at half maximum (FWHM) of the diffraction peak and θ corresponding to the peak position.

The X-ray photoelectron spectra (XPS) were collected on an Omicron Argus X-Ray photoelectron spectrometer using a monochromatic Al Kα radiation ($h\nu$ = 1486.6 eV) with a 300 W electron beam power. The emission of photoelectrons from the sample was analyzed at a takeoff angle of 45° under ultra-high vacuum conditions (1 x 10^{-8} Pa). XP spectra were collected at pass energy of 20 eV for C 1s, Si 2p, Ni 2p and O 1s core XPS levels. The charging effects were corrected by adjusting the binding energy of the C 1s peak from carbon contamination to 284.8 eV. The peak areas were

determined after subtraction of a Shirley background. The atomic ratio calculations were performed after normalization using Scofield factors. Spectrum processing was carried out using the Casa XPS software package.

Thermogravimetric analyses (TGA) were performed in order to quantify the amounts of carbon deposited on the spent catalysts using a TA SDT Q600 thermal analyzer instrument. Measurements were carried out from R.T. to 900°C (heating rate 10°C min^{-1}) in flowing air (100 mL min^{-1}).

Temperature-Programmed Reduction (TPR), carried out on Autochem 2910 or 2920 (Micromeritics) instruments equipped with TCD detectors, was used in order to study the nickel reducibility of the calcined materials. The samples (80 mg) deposited on a plug of quartz wool in a U-shaped quartz tube were heated from R.T. to 900 °C at a rate of 10°C min^{-1} using a 5 vol% H_2/Ar gaseous mixture (25 mL min^{-1}). An isopropanol-liquid N_2 mixture (Autochem 2910) or an ice and salt bath (Autochem 2920) were placed before the TCD detectors to trap the water molecules formed during NiO reduction. The nickel loading was deduced from the amount of H_2 consumed during the TPR experiment after controlling that the Ni loading of a reference material was found to be coherent with that determined by inductively-coupled plasma optical emission spectrometry (ICP-OES, Crealins-Villeurbanne). The Autochem 2910 and 2920 instruments were also used to perform high-temperature H_2 reductions mimicking the *in-situ* reduction (detailed later) carried out as a pretreatment step prior to the catalytic test.

Transmission Electron Microscopy (TEM) analyses were performed on a JEOL-1011 (LaB6) and JEOL-2010 (LaBs) microscopes operating at 200 kV. The sample powder was ultrasonicated in ethanol and several drops of the resulting suspension were deposited on a copper grid coated with a porous carbon film. Observations were made once ethanol was evaporated at R.T. For the solids prepared by ultramicrotome, transmission electron microscopy (TEM) images and HRTEM images were taken on a JEOL JEM-2010 UHR operating at 200 kV, equipped with an EDX detector. A few mg of powder were deposited in the bottom of a Beam capsule. Some embedding resin (AGAR 100) was added and polymerized for 48 h at 60°C. The polymerized blocks were then cut into ultrathin sections (about 70 nm thick) using a diamond knife of a Leica microtome (ULTRACUT UCT) and deposited on carbon-coated copper grids.

To observe nickel dispersion and location, STEM/HAADF and EDX/mapping were also performed on a JEOL 2020 microscope on ultra-thin sections of selected samples.

The 3D imaging by electron tomography was performed in the scanning transmission electron microscopy (STEM) mode using a JEOL 2100 FEG STEM microscope operated at 200 kV and equipped with a probe spherical aberration corrector. The sample was dispersed in ethanol and deposited on a holey carbon-coated TEM grid. For the acquisition of the STEM-HAADF (high angular annular dark field) images, a spot size of 0.13 nm, a current density of 140 pA and a camera length of 8 cm (corresponding to inner and outer diameters of the annular detector of about 73 and 194 mrad), were used. The acquisition of tilt series was recorded using the tomography plug-in of the Digital Micrograph software, which controls the specimen tilt step by step, the defocusing and the specimen drift. The spatially correlated HAADF and BF tilt series were acquired by using the ADF and BF detectors and tilting the specimen in the angular range of ± 66° using an increment of 2° in the equal mode, giving thus 65 images in each series. These images were spatially aligned by using a cross correlating algorithm; the volume reconstruction was subsequently calculated using the algebraic reconstruction technique (ART) of the TomoJ plugin implemented in the ImageJ software. Finally, the visualization and the analysis of the 3D reconstructions were carried out using the displaying capabilities and the isosurface rendering method of the Slicer software.

H_2 Chemisorption experiments were performed on a BELSORB-max equipment from BEL JAPAN. The samples (about 200 mg) were reduced in situ under a flow of H_2 (50 mL min^{-1}) at 650°C for 2 h using a ramp of 10°C min^{-1}. The sample was then outgassed at 620°C for 2 h under vacuum (about $5x10^{-5}$ Pa). Firstly, H_2 chemisorption measurement was performed at 25°C, the pressure at equilibrium being recorded when the pressure variation was below 0.02% per minute. The sample was then outgassed for 2 h at 25°C before a second H_2 chemisorption was performed under the conditions described before. Nickel particle size estimations are based on truncated octahedron geometry, assuming complete reduction, semi spherical particles and a H/Ni adsorption stoichiometry factor of 1. The experimental data were fitted with a Langmuir adsorption equation (Equation 1) and the amount of surface nickel was calculated from the quantity

adsorbed at saturation (Q_{max} in the model). The dispersion refers here to as the molar percentage of surface Ni atoms compared to the total number of Ni atoms in the sample.

$$\theta = \frac{Q_{\text{ads}}}{Q_{max}} = \frac{\sqrt{KP}}{1+\sqrt{KP}} \quad \text{(Equation 1)}$$

θ: Fractional occupancy of the adsorption sites
Q_{ads}: Quantity adsorbed
Q_{max}: Quantity adsorbed on saturation
K: Equilibrium constant
P: Partial pressure of the adsorbate

Pair Distribution Function (PDF) analysis

The reduced atomic PDF, G(r), gives, from a structural model, the probability of finding a pair of atoms at a distance of r as follows:

$$G(r) = 4.\pi.r.\ [\rho(r) - \rho_0], \text{ (Equation 2)}$$

where ρ(r) is the atomic pair-density and ρ_0 is the average atomic number density. As defined, peaks in the G(r) function correspond to specific distances separating pairs of atoms.

G(r) can also be extracted from an experimental XRD pattern. Indeed, G(r) is the Fourier transform of the total structure function S(Q):

$$G(r) = \left(\frac{2}{\pi}\right) . \int_{Q=0}^{\infty} Q.[S(Q) - 1].\sin(Qr)dQ, \text{ (Equation 3)}$$

where Q is the magnitude of the scattering vector ($Q = 4\pi\sin\theta/\lambda$), 2θ being the angle between the incoming and outgoing X-ray, λ is the X-Ray wavelength, and S(Q) is the total scattering structure function which is the corrected and normalized experimental intensity.

The X-Ray scattering measurements were performed on a Brüker D8 Advance diffractometer equipped with a molybdenum anode, a Göbel mirror and a High Energy Lynx Eye linear detector. The analysis was done in transmission: a few milligrams of powders were placed in a borosilicate capillary of 1 mm diameter that was sealed. To optimize the acquisition time, the X-Ray diagrams used for the PDF were obtained by concatenation of 7 X-Ray diagrams recorded with the following parameters ($2\theta_i$ (°)-$2\theta_f$ (°)-step (°)-time per step (s): 0.8-31-0.02-2, 29-61-0.04-6, 59-91-0.06-15, 89-121-0.1-40 (2 times), 119-150-0.1-100 (2 times). The XRD of the empty capillary was also recorded for subtraction. Then, the PDFGetX3 software [28] was used to extract the experimental PDFs from XR diagrams (Q_{min}=0.7; Q_{max}=16.6; rpoly=1.3). In parallel,

the PDFGUI software [29] was used to calculate the theoretical function G(r) from a structural model. For comparison purposes, experimental G(r) were normalized so that all experimental G(r) present a first peak (dSi-O=1.6 Å) at the same intensity.

II.3 Catalytic measurements

The different catalysts were tested using a PID ENG & TECH Microactivity Effi Reactor. The solids were loaded on a plug of quartz wool and treated in-situ at 650°C for 2 h (10°C min^{-1}) in a 5 vol.% H_2/Ar flow (30 mL min^{-1}) in order to achieve a complete reduction of NiO into metallic nickel. After this pretreatment step, the temperature was decreased to 200°C and the dry reforming of methane reaction was started under atmospheric pressure, using a CH_4/CO_2/Ar (0.5/0.5/9) reacting mixture and a total Gas Hour Space Velocity (GHSV) of 144 (50 mg of catalyst and 120 mL min^{-1} total flow) or 960 L g^{-1} h^{-1} (10 mg of catalyst diluted with 90 mg of fumed silica (Aldrich 381276) and 160 mL min^{-1} total flow of reactants mixture). The GHSV values, which can also be calculated on the basis of the Ni weight of the catalysts, are 2880 and 3840 L g^{-1} h^{-1}, respectively.

Firstly, the activity of the catalyst was measured by increasing the reactor temperature from 200 up to 650 °C (using a rate of 5 °C min^{-1}). The temperature was then maintained at 650 °C for 12 h for stability measurements. The gaseous products were analyzed online by a micro-GC (Agilent 490) equipped with Plot-U and Molecular sieves columns using a TCD detector. The conversions of methane and carbon dioxide were calculated according to Equations 4 and 5, respectively, and the H_2/CO ratios were estimated using Equation 6:

$$CH_4 \text{ conversion, } \% = \frac{(CH_{4(in)} - CH_{4(out)})}{CH_{4(in)}} \times 100 \quad \text{(Equation 4)}$$

$$CO_2 \text{ conversion, } \% = \frac{(CO_{2(in)} - CO_{2(out)})}{CO_{2(in)}} \times 100 \quad \text{(Equation 5)}$$

$$H_2/CO = \frac{H_{2(out)}}{CO_{(out)}} \quad \text{(Equation 6)}$$

The reproducibility of the catalytic tests was evaluated by double testing chosen catalysts. The latter were considered reproducible when the difference between the two

repetitions did not exceed 5% (for CH_4 and CO_2 conversions) and 0.05 (for H_2/CO molar ratio) maximum.

III. Results and discussion

The calcined and reduced solids will be characterized separately and then the reactivity of reduced materials will be evaluated under different DRM conditions.

III.1 Calcined samples

All the samples (2.5 and 5 wt.% Ni) prepared either by impregnation or one-pot insertion of Ni are characterized by type IV isotherms forming a H1 hysteresis loop typical of mesoporous materials with a narrow range of uniform mesopores (Fig. 1A and S2) [30]. Upon impregnation with the aqueous solution of $Ni(NO_3)_2.6H_2O$, the pore volume of the support (S) did not change to a significant extent for $Ni^{II}_{2.5\%}$/S and $Ni^{II}_{5\%}$/S samples (Table 1). A similar conclusion can be drawn regarding the evolution of the specific surface area after Ni impregnation with a decrease of 9.6 and 11.6% for $Ni^{II}_{2.5\%}$/S and $Ni^{II}_{5\%}$/S, respectively. The mean pore diameter (5.4 nm) was found to remain essentially constant before and after impregnation. In contrast, it must be noticed that $Ni^{II}_{2.5\%}$@S and $Ni^{II}_{5\%}$@S solids prepared by one-pot synthesis exhibited higher specific surface areas but lower pore volumes compared to those of the $Ni^{II}_{2.5\%}$/S and $Ni^{II}_{5\%}$/S reference samples.

Figure 1

Finally, the mean pore diameters of the samples prepared by one-pot synthesis were found to be about 1 nm smaller compared to those of the samples prepared by impregnation (Table 1).

Table 1

In good agreement with the N_2 sorption data, small angle X-Ray diffractograms of selected calcined samples (Fig. 1B) exhibited the (100), (110) and (200) peaks characteristic of highly-ordered hexagonal mesoporous materials with a P6mm structure [31]. This observation proves the high organization of the pores in the prepared SBA-15 monoliths. It is noteworthy that the intensity of the (110) and (200) peaks decreases in the case of $Ni^{II}_{5\%}$/S probably due to the lower long range order

induced by the presence of NiO inside the porosity. Undoubtedly, the $Ni^{II}_{5\%}$@S sample was characterized by a greater pores structuration compared to that of $Ni^{II}_{5\%}$/S.

Wide angles X-Ray diffractograms of the calcined $Ni^{II}_{5\%}$/S samples (Fig. S3) show five diffraction peaks at 2θ° = 37.2, 43.3, 62.9, 75.4 and 77° (★). These contributions were assigned to the (111), (200), (220), (311) and (222) crystallographic planes of NiO particles with a face-centered cubic lattice (Fm-3m, JCPDS no. 89-7130) [32]. The mean NiO particle size for $Ni^{II}_{5\%}$/S is estimated to be about 6 nm from the Scherrer equation, which is similar to the mean pore diameter of the corresponding support (Table 1). In contrast, no peak indicative of the presence crystalline NiO particles could be observed for $Ni^{II}_{5\%}$@S, which suggests the formation of small nanoparticles and/or of clusters with the one-pot strategy. Similar observations were made in the case of $Ni^{II}_{2.5\%}$-S solids (Fig. S4).

The reducibility of the nickel species was investigated by H_2-TPR and the Ni loadings were also deduced from these measurements (Fig. 2 and Table 1).

Figure 2

Overall, the reduction profile of the sample prepared through post-synthesis impregnation was found to be very different from the one obtained by the one-pot strategy. $Ni^{II}_{5\%}$/S exhibited two reduction peaks at 400 and 620°C and was fully reduced at 710 °C (Fig. 2). The H_2 consumption at c.a. 400°C is usually attributed to the large NiO particles (bulk) with low metal-support interaction [33], whereas the H_2 consumption at c.a. 600°C can be assigned to smaller NiO species in stronger interaction with SiO_2. It is noteworthy that the high-temperature reduction peak (640°C) becomes the major contribution in the case of the $Ni^{II}_{5\%}$@S sample and full reduction of this solid was achieved at a higher temperature (~ 800°C) compared to the material prepared by impregnation (710°C). Such differences in reduction behavior between those materials, having similar Ni loadings, highlight the strong influence of the preparation method on nickel reducibility. The one-pot pathway would improve the metal-support interaction, thus leading to the formation of smaller Ni^0 NPs during the reduction step [34, 35]. Likewise, TPR analyses were conducted for $Ni^{II}_{2.5\%}$/S and $Ni^{II}_{2.5\%}$@S solids in order to confirm this hypothesis. Figure S5 reflected comparable behaviors (two peaks and lower metal support interaction for $Ni^{II}_{2.5\%}$/S obtained via

post-impregnation vs. one main peak and higher metal support interaction for $Ni^{II}_{2.5\%}$@S prepared through the one-pot strategy). Thus, it is obvious that the one-pot preparation method indeed promotes the Ni-SiO_2 interaction. A comparison of the Ni's reducibility (using relatively close H_2-TPR operating conditions) between relevant examples of Ni-SiO_2 based catalysts designed by using either impregnation, a core-shell approach or a colloidal pathway while excluding materials based on Ni phyllosilicates or involving promoters is proposed in Table S1. Beside the colloidal pathway, whatever the impregnation method used, two reduction peaks are often identified in good correlation with what we observed for $Ni_{5\%}$/S. The particles size control afforded by the colloidal pathway could explain the "one reduction peak" behavior of the corresponding catalysts. The one-pot method developed throughout the present study has led, so far, to one main reduction peak at relatively high reduction temperature when compared to its counterparts (Ni/S samples here or other catalysts in Table S1). Accordingly, these results stressed the advantage of the one-pot pathways towards improving the metal-support interaction as well as, probably, particle size control.

In addition, the Ni loadings of the different samples were estimated from the quantities of H_2 consumed in the NiO to Ni reduction. Table 1 shows that the estimated Ni loadings for all of the prepared solids is relatively close to that expected, in particular for the one-pot prepared samples.

An appropriate way to monitor the interaction of Ni with the support consists in studying the materials by XPS. Two representative XPS spectra recorded on the $Ni^{II}_{5\%}$/S and $Ni^{II}_{5\%}$@S samples are shown in Fig. 3.

Figure 3

Both solids exhibited two main peaks corresponding to Ni $2p_{3/2}$ and Ni $2p_{1/2}$ core levels with their shake up satellites that are clearly different. The Ni $2p_{3/2}$ peak for $Ni^{II}_{5\%}$/S could be decomposed into two contributions at 853.8 and 856.0 eV that have been already observed for bulk-scale and nano-sized polycrystalline NiO up to 5 nm [36]. Nickel oxide supported onto silica is also often characterized by binding energy values between 853 and 855 eV and usually, it is believed that the stronger nickel oxide interacts with silica, the more the peaks are shifted to higher energy values. In the case

of $Ni^{II}_{5\%}$@S, a major contribution was observed at approximately 857 eV with a very small one at 853.8 eV as reported in the work of K.O. Sebakhy et al [37] dealing with highly dispersed Ni within silicate zeolites. In some studies, it is mentioned that this could be also the result of the presence of Ni(III), but this is not compatible in our case with the quantification of nickel by TPR-H_2 shown before. As the result, we believe that the XPS spectrum of $Ni^{II}_{5\%}$@S is more compatible with tiny NiO nanoparticles (clusters) or nickel(II) silicate or nickel(II) hydroxide [38] but the pH range of the synthesis gel is not appropriate for the formation of silicates or hydroxides. NiO clusters could also be present in $Ni^{II}_{5\%}$/S but to a lesser extent. A similar trend was also observed in the case of Ni $2p_{1/2}$ peaks. Those XPS results are coherent with the observations made by TPR in which $Ni^{II}_{5\%}$/S showed two main reduction peaks (Fig. 2). Based on the areas of the two contributions in H_2-TPR (at 400 and 620°C, Fig. 2) and XPS (at 853.8 and 856.0 eV, Fig. 3), the first one can be assigned to NiO particles with low metal-support interactions, whereas the second one can be attributed to NiO clusters with stronger interaction with the silica support. $Ni^{II}_{5\%}$@S mainly exhibited Ni^{2+} species strongly interacting with the silica support as indicated by the corresponding H_2-TPR trace (Fig. 2) and XPS spectra (Fig. 3). In addition, the XPS Ni/Si atomic ratios were estimated to be 0.03 and 0.01 for $Ni^{II}_{5\%}$@S and $Ni^{II}_{5\%}$/S, respectively. These Ni/Si ratios, especially for $Ni^{II}_{5\%}$/S, were found to differ from the theoretical ratio (0.05). In our opinion, such XPS data would be coherent with the better Ni dispersion for the solid prepared by means of the one-pot method ($Ni^{II}_{5\%}$@S) compared to that prepared by post-synthesis impregnation ($Ni^{II}_{5\%}$/S).

The calcined $Ni^{II}_{5\%}$-S samples were also characterized by TEM in order to investigate the dispersion and the location of Ni species (Fig. 4).

Figure 4

TEM micrographs of $Ni^{II}_{5\%}$/S provide further support for the presence of i) an ordered hexagonal mesoporosity of the support, in good agreement with the N_2 sorption isotherms and small angles X-Ray diffraction data (Fig. 1), and ii) NiO particles (Figs. 4A, A' and B). Indeed, using Selected Area Electron Diffraction (SAED), the five rings made of small spots observed for $Ni^{II}_{5\%}$/S (Fig. 4C) indicate the presence of polycrystalline NiO ((111), (200), (220), (311) and (222) crystalline planes of the fcc

lattice) with a crystallographic distance, d_{200}, of 2.08 Å. Furthermore, in this sample (prepared by post-synthesis impregnation), the observed rows of NiO nanoparticles (Figs. 4A and A') were not homogeneously distributed. Regarding $Ni^{II}_{5\%}$@S, it is worth mentioning that the addition of Ni in the synthesis gels did not affect the structuration of the silica's pores to a significant extent (Figs. 4D and F) as its mesoporosity seems to be essentially preserved. In agreement with the wide angles XRD (Fig. S3), NiO particles were very difficult to observe in $Ni^{II}_{5\%}$@S (Figs. 4D, E and F) compared to $Ni^{II}_{5\%}$/S (Figs. 4A, A' and B). It is worthwhile to know that the TEM images for the solids loaded with 2.5 wt.% Ni (Fig. S6) revealed similar observations.

These TEM observations (Figs. 4 and S6) agreed with i) the absence of wide angles XRD peaks (Figs. S3 and S4) and ii) the much lower Ni/Si XPS ratio. Moreover, the fact that the H_2-TPR profiles are shifted to higher reduction temperatures (Fig. 2 and S5) for the samples prepared by a one-pot protocol (Ni^{II}@S) is coherent with the formation of much smaller NiO nanoparticles and/or the presence of highly dispersed Ni^{2+} ions in greater proportion in the one-pot samples.

Using PDF analyses, more information on the structure and the particle size of the Ni species in $Ni^{II}_{5\%}$@S can be obtained even in the absence of X-Ray diffraction peak. This technique consists in the analysis of the total X-Ray scattering by ways of Fourier Transform that leads to the $G_{exp}(r)$ function [28]. $G_{sim}(r)$, a similar function can be calculated from a proposed structural model as the probability of finding a pair of atoms separated by the distance r [29]. Comparison of $G_{sim}(r)$ and $G_{exp}(r)$ leads to the validation of the proposed structural model and also allows for checking the nickel oxidation state (Fig. 5A). Indeed, the first 3 characteristic simulated peaks stand at 2.1, 3.1 and 5.3 Å for NiO, and at 2.48, 3.52 and 4.30 Å for Ni^0. As expected, $G_{exp}(r)$ curve for calcined $Ni^{II}_{5\%}$@S (Fig. 5B) mainly shows silica (1.6; 2.1; 2.6; 3.0 Å…). However, the superposition of $G_{exp}(r)$ for calcined $Ni^{II}_{5\%}$@S with $G_{exp}(r)$ of the corresponding support, S, reveals three differences of the intensities at 2.1, 3.1 and 5.3 Å matching with NiO peaks. The next expected NiO peak at 6.61 Å is not observed nor the following others, meaning that the limit of the atom correlation is reached for these distances. From these results, we can conclude that nickel in $Ni^{II}_{5\%}$@S is most likely present as NiO clusters with an average size of about 6 Å in diameter.

Figure 5

STEM/HAADF and TEM combined with EDX/mapping carried out on $Ni^{II}_{5\%}$@S confirmed that nickel is present as highly dispersed species on the siliceous support (Fig. 6). Similar information could also be obtained with EDX analyses (data not shown) performed on several regions of the $Ni^{II}_{5\%}$@S sample.

Figure 6

III.2 Reduced samples

The full reduction of the SBA-15-supported Ni samples was achieved after exposure to H_2 at 650°C for 2 h, as verified by H_2-TPR (results not shown here).

The shapes of the N_2 sorption isotherms and of the hysteresis loops of $Ni^0_{5\%}$@S and $Ni^0_{5\%}$/S samples (Fig. S7) were found to be relatively similar to those of their calcined precursors, i.e. $Ni^{II}_{5\%}$@S and $Ni^{II}_{5\%}$/S (Figs. 1A and S2). Hence, the BJH treatment of the isotherms revealed that the mean pore diameters and the pore size distributions of $Ni_{5\%}$@S or $Ni_{5\%}$/S are almost the same before and after the reduction step. However, a decrease in the specific surface areas (Table S2, -25 and -17%, respectively) could be observed in parallel with the decrease of the contribution of micropores to the total pore volume. Such a change, which was not significant after the calcination of $Ni^{II}_{5\%}$-S precursors, would be attributed to the condensation of the micropores under high-temperature thermal treatment (here 2 h at 650°C).

After reduction of $Ni^{II}_{2.5\%}$/S and $Ni^{II}_{5\%}$/S, prepared by impregnation of S, the diffraction peaks of NiO crystallites observed before (Figs. S3 and S4) disappeared, whereas new diffraction peaks characteristic of the presence of Ni^0 nanoparticles (JCPDS n° 70-1849) [39] appeared at $2\theta = 44°$ (111), 52° (200) and 76° (220) (Figs. S8 and S9).

For $Ni^0_{5\%}$/S, the size of these Ni^0 nanoparticles is estimated, from the Scherrer equation, to be close to 7-8 nm, which is found to be slightly bigger than the pristine NiO particles (~ 6 nm). Since the density of NiO crystallites (6.6 g cm^{-3}) is lower than that of Ni^0 crystallites (8.3 g cm^{-3}), such an increase in Ni^0 particles size can be attributed to moderate sintering of the Ni particles during the reduction step. On the other hand, no X-Ray diffraction peaks characteristic of Ni^0 were observed for the reduced forms of the one-pot prepared Ni@S samples (Figs. S8 and S9) suggesting the presence of very small and highly dispersed nanoparticles in these materials.

TEM micrographs of the reduced solids (Fig. 7) firstly confirmed the preservation of the ordered porosity after the reduction treatment. As it was the case for the NiO particles in calcined $Ni^{II}_{5\%}$/S (Figs. 4A, A' and B), Ni^0 particles with relatively heterogeneous dispersion were easily observed in $Ni^0_{5\%}$/S (Figs. 7A and A'). Most of these particles were still located inside the porosity but it could be noticed that some of them (Fig. 7B, white circles) seem to have damaged locally the silica pore walls. The mean Ni^0 particle size for $Ni^0_{5\%}$/S was estimated to be 8.0 nm from the TEM images (Table 1) in good agreement with the size that was estimated by XRD (Fig. S8).

Figure 7

For $Ni^0_{5\%}$@S (Fig. 7C and D), a few particles of a size close to the pore diameter (about 5-6 nm) could be easily observed (Fig. 7C) but, using a higher magnification, many other smaller nanoparticles, with an average size of about 2.1 nm (Table 1), were also found in the mesoporosity of the support (Fig. 7D). The $Ni^0_{5\%}$@S solid was also analyzed by PDF in order to confirm the complete reduction of the NiO particles and to estimate the size of Ni^0 NPs obtained (Fig. S10).

Indeed, Figure S10 shows 4 peaks at 2.5, 4.2, 6.5 and 9 Å that can be attributed to the presence of Ni^0 NPs with a mean particle size of about 1 nm, while no NiO contribution could be detected.

To reach a more reliable insight on the microstructure of the catalyst grain as well as on the relative distribution and localization of the Ni-based nanoparticles, we have analyzed two typical grains of $Ni^0_{5\%}$@S by electron tomography in the STEM-HAADF mode. The obtained results are depicted in Figs. 8 and S11.

Figure 8

By analyzing the reconstructed volumes slice by slice, we easily observe that most of the nanoparticles can be found in the inner part of the catalyst grain and very few are close to the external surface. Within the aggregate, the particles are very well distributed and attached to the pore walls, most of them having a nanometric size (about 1 nm) and only very few (denoted by the red arrows in Fig. 8 C) a size close to the pore diameter. Another important finding obtained from the tomography analysis concerns the influence of the long range order of the mesoporous structure on the distribution

and final size of the Ni nanoparticles. By comparing the characteristics of the particles localized in a very ordered region and in a less ordered one respectively (corresponding to the left and right areas of the 3D volume depicted in Figure 8 B), we can easily observe that the size of the particles in the area characterized by a long range order of the porosity is smaller, which demonstrates the beneficial effect of the mesoporous order on the final structural properties of the Ni-based catalyst.

The estimation of the Ni dispersion from Ni-silica samples by H_2 chemisorption is far from being trivial. Bartholomew recommended that it should be done on the basis of the first H_2 isotherm (including reversibly and irreversibly chemisorbed hydrogen) [40]. Indeed, he argued that reversible hydrogen chemisorption takes place on Ni crystallites rather on the support, support contaminant, or unreduced Ni. This conclusion was supported by the good agreement obtained between H_2 chemisorption, XRD and TEM data. The reversible hydrogen chemisorption phenomenon on Ni could be due to the much weaker bonding of hydrogen on some Ni sites compared to those of Pt group metals, which thus prevents the use of the back sorption method on Ni samples. Yet, studies performed on Ni catalysts can be found for which the metal dispersion was estimated by the back sorption method therefore only taking into account irreversibly chemisorbed hydrogen [41]. Doing the same in our case, the estimated Ni mean particle size for $Ni^0_{5\%}$/S and $Ni^0_{5\%}$@S (55 and 8.6 nm, respectively) were found to differ markedly from those obtained by XRD and/or TEM (7-8 and 2.1 nm). Although it was checked in the present work that the support alone showed reversibly adsorbed hydrogen species (0.3430 $cm^3\ g^{-1}$), the data listed in Table 2 are related to the amounts of hydrogen adsorbed in the first H_2 isotherm, thus to the total (reversible + irreversible) hydrogen uptake. This method was selected for comparison purpose as most of the Ni dispersion data reported to date on silica-supported catalysts used in the DRM reaction were obtained likewise (Table S3 and references included).

Table 2

Table 2 shows that, for $Ni^0_{5\%}$/S, the Ni particles size estimated by H_2 chemisorption (12.6 nm) is in rather good agreement with those obtained by XRD (7-8 nm) and TEM (8.0 nm, Table 1). We hypothesize that the over-estimation with H_2 chemisorption can be attributed to differences in the accessibility of hydrogen to the Ni sites given that $Ni^0_{5\%}$/S was shown to exhibit some bundles of Ni^0 particles by TEM (Fig. 7). On the

other hand, the estimated particles size for $Ni^0_{5\%}$@S (about 3 nm) is in better agreement with those obtained by TEM and PDF (2.1 and ~ 1 nm, respectively). It is also consistent with the absence of XRD contributions for these reduced samples (Fig. S8). In that case, the agreement between the Ni particles size estimated by H_2 chemisorption and TEM may be assigned to a much better accessibility of the Ni surface sites compared to $Ni^0_{5\%}$/S. The Ni dispersions in $Ni^0_{5\%}$/S and $Ni^0_{5\%}$@S samples were estimated in parallel from H_2 chemisorption data and TEM. In the latter approach, the volume-area mean diameters (defined by $d_{VA} = \Sigma n_i d_i^3 / \Sigma n_i d_i^2$) were deduced to be 2.9 and 8.5 nm for $Ni^0_{5\%}$@S and $Ni^0_{5\%}$/S, respectively. The metal dispersions (calculated as $D = 6 \frac{(v_{Ni}/a_{Ni})}{d_{VA}}$, where v_{Ni} is the volume occupied by a Ni atom in the bulk (v_{Ni} = 10.95 Å^3) and a_{Ni} is the surface area occupied by a Ni atom on a polycrystalline surface (a_{Ni} = 6.51 Å^2) [42]), were estimated to be 35% and 11.7% for $Ni^0_{5\%}$@S and $Ni^0_{5\%}$/S, respectively. Such values are in very good agreement with those obtained from the H_2 chemisorption technique listed in the Table 2. It is worthwhile to note that the Ni dispersion in $Ni^0_{5\%}$@S prepared by the one-pot method is among the best dispersion values reported to date for silica-supported nickel (Table S3 and references included). Finally, it can also be noted that $Ni^0_{2.5\%}$@S had a slightly higher dispersion of Ni than $Ni^0_{5\%}$@S (Table 2).

Hence the present one-pot strategy used to prepare the Ni@S samples with a high Ni loading and a good dispersion is found to be very simple and cost-effective compared to other methods described earlier in the literature aiming at controlling the Ni particle size confined in porous supports (Table S3 and references included).

III.3 Catalytic DRM performance and spent sample characterization

The catalytic performance of the *in situ*-reduced $Ni^0_{5\%}$@S catalyst was investigated firstly in the DRM reaction under a GHSV of 144 L g^{-1} h^{-1}. As expected the conversions of CH_4 and CO_2 rise when increasing the temperature (Fig. 9A). Under these conditions, $Ni^0_{5\%}$@S was found to be very active, with CH_4 and CO_2 conversions (~ 75% at 650°C) close to the thermodynamic equilibrium values (85 and 89 % for CH_4 and CO_2, respectively) determined in the absence of carbon formation, and highly stable during 12 h allowing the selective formation of H_2 and CO (molar H_2/CO close to 1 (Fig. 9B)). Secondary reactions did not occur to a large extent in agreement with the

observed fairly good stability of the catalyst. Similar results were obtained too with $Ni^0_{2.5\%}$@S (results not shown).

After use, the spent $Ni^0_{5\%}$@S material was characterized by N_2 sorption, XRD, TGA and TEM techniques (Figs. S7, S12 and S13) in order to monitor the eventual changes of the textural properties, crystallinity and Ni dispersion as well as coke deposition under the DRM reaction operating conditions. N_2 sorption data (Fig. S7) indicated that the shape of the isotherms of the spent sample compared well with those of the reduced $Ni^0_{5\%}$@S starting material. After 12 h on stream, the specific surface area and the pore volume of the spent sample were found to be preserved (Table S2), thus confirming the good stability of the monolith support during the catalytic test.

Figure 9

TGA analysis of the spent $Ni^0_{5\%}$@S sample (Fig. S12A) does not reveal the presence of carbon deposits, thus indicating, in agreement with the H_2/CO molar ratio close to 1 (Fig. 9B), the limited involvement of secondary reactions. This result also shows that the Ni particles did not sinter to a significant extent, in agreement with the absence of Ni^0 diffraction peak (Fig. S12B) under the DRM reaction operating conditions. It was also impossible to conclude on the potential conversion of Ni into nickel carbides too.

The absence of Ni sintering was verified by TEM and STEM/mapping (Fig. S13), which allowed us to conclude that the mean Ni particle size is close to 2.7 nm on the spent sample. The fact that this sample was little affected by carbon deposition, as indicated by the TGA data (Fig. S12A), is consistent with the presence of the very small Ni particles observed by TEM (Fig. S13) as it has been reported that coke deposition was favored on large Ni particles [43].

Following these preliminary experiments, the catalytic performances of $Ni^0_{5\%}$/S and $Ni^0_{5\%}$@S were investigated under a kinetic regime (GHSV = 960 L g^{-1} h^{-1}, dilution with silica) far from the thermodynamic equilibrium of the DRM reaction (Figs. S14 and 10) in order to allow a reliable comparison and the determination of the Turn-Over Frequency (TOF) values of these catalysts. Regardless of the parameters that could affect the TOFs such as (i) the determination mode of the Ni dispersion, (ii) the composition of the reacting feed (iii) the reacting temperature used, (iv) the conversion

values, (v) the presence of promoters and/or other metals, etc, the values found for our catalysts were similar or even superior to those of most of Ni-Silica based ones reported for the DRM (between 0 and 2 s^{-1}) [44-45, see also other references in Table S4] even if there are still some higher values reported (> 10 s^{-1}) by some groups [1, 7, 14, 46-47, see Table S4]. We think, however, that the preparation method described in the present work is easy and cost-effective (no bimetallic and promoters) when compared to some of the aforementioned studies.

At 650°C, $Ni^0_{5\%}$@S was found to be a more active and selective DRM catalyst than $Ni^0_{5\%}$/S with CH_4 and CO_2 conversion values around 48% (and 45% for the reproducibility test) instead of c.a. 25% (CH_4) and 29% (CO_2) (Fig. 10 A) and a H_2/CO molar ratio close to unity. Moreover, the stability of $Ni^0_{5\%}$/S at 650°C was found to be very limited as the CH_4 and CO_2 conversions decreased drastically to about 0% within 4 h on stream and the H_2/CO molar ratio from about 0.8 to 0 within 10 h (Fig. 10B).

Figure 10

These results clearly illustrate the superiority of the Ni catalyst prepared by the one-pot method compared to that obtained by post-synthesis impregnation (TS method). Such a difference is attributed undoubtedly to the presence of much smaller size sintering- and coke-resistant Ni^0 particles in Ni@S samples. For confirmation, $Ni^0_{2.5\%}$@S was also tested with a GHSV value of 960 L g^{-1} h^{-1} at 650°C and, despite a lower Ni loading than that of $Ni^0_{5\%}$/S, $Ni^0_{2.5\%}$@S exhibited similar catalytic performance (Fig. S15) while $Ni^{\mathbf{0}}_{2.5\%}$/S led to very low CH_4 and CO_2 conversions (not shown). The CH_4 and CO_2 conversions for $Ni^0_{2.5\%}$@S and $Ni^0_{5\%}$/S were found to be around 30% but $Ni^0_{2.5\%}$@S led to a better H_2/CO selectivity (much closer to 1). Moreover, $Ni^0_{2.5\%}$@S, alike $Ni^0_{5\%}$@S, was shown to be very stable for 12 h on stream (Fig. S16A) maintaining a H_2/CO molar ratio close to 1 (Fig. S16B). It can also be noticed that the CO_2 and CH_4 conversion values with $Ni^0_{5\%}$@S were almost twice as high as those obtained with $Ni^0_{2.5\%}$@S (45 and 25%, respectively). Considering i) that the catalyst loading in the reactor was maintained to 10 mg in both experiments ($Ni^0_{2.5\%}$@S and $Ni^0_{5\%}$@S) and ii) that $Ni^0_{2.5\%}$@S displayed about half of the Ni content of $Ni^0_{5\%}$@S (Table 1) with a slightly greater Ni dispersion (35 compared to 31%, respectively), such observation confirms that $Ni^0_{5\%}$@S and $Ni^0_{2.5\%}$@S were operated under a true kinetic regime. This,

thus, resulted in close TOF values for both samples (Table 1) without any significant evolution after 12 h on the contrary to those of $Ni^0_{5\%}/S$.

TEM analyses of spent $Ni^0_{5\%}/S$ (Fig. S17) were performed in order to understand the origin of its strong deactivation in the DRM at 650°C (Fig. 10). Resulting micrographs revealed that the porosity and the organization of the support were globally maintained after 12 h. However, two types of Ni particles could be detected, i.e. small ones still confined in the silica mesoporosity (with a size distribution of about 5-7 nm) and, much bigger ones located on the outer surface of the support (with sizes of about 17-22 nm) that should have been formed through migration and sintering phenomena. The resulting mean Ni^0 particle size in spent $Ni^0_{5\%}/S$ was estimated to be 11.8 nm. Furthermore, no structured carbon species such as carbon nanotubes could be observed on the spent $Ni^0_{5\%}/S$ diluted with silica after 12 h on stream but we cannot exclude that amorphous carbon is formed. The dilution of the catalysts (10 mg of $Ni^0_{5\%}/S$ with 90 mg of silica) required to test their activity under these conditions and the low contrast of carbon in TEM measurements result in no meaningful conclusion as to whether or not amorphous carbon is present. Moreover, accurate TGA and XRD analyses of the spent $Ni^0_{5\%}/S$ could not be carried out too.

In heterogeneous catalysis, electronic effects related to the supports can occur. Some studies have already reported support effects for the Ni-catalyzed dry reforming reaction and this is generally proven by active phase reducibility measurements that are evaluated by TPR-H_2 material analysis [48]. Reduction on SiO_2 occurs generally in between 300°C and 500°C. Here, in the case of $Ni^0_{5\%}$@S, it occurs at much higher temperature in agreement with the presence of nickel oxide clusters that are more difficult to reduce [18].

IV. Conclusion

The existing literature dealing with the use of SBA-15 silica as a support for the preparation of nickel-based catalysts for the DRM reaction is flourishing, but when restricted to studies not involving metallic or oxide promoters, much less articles remain in which nickel is most often introduced by impregnation processes. An

example of nickel introduction of nickel into the synthesis gel of a SBA-15 silica prepared in citric acid was reported by Q. Liu et al, but the porosity was greatly affected and resulting nickel particles were much less dispersed than ours [49]. The aim of this work was to design stable and well-dispersed Ni-silica based catalysts using an easy preparation method. This objective was achieved through an original sol-gel one-pot strategy tested with 2.5 and 5 wt.% of Ni. Calcined solids, thus obtained, are characterized by highly dispersed nickel species (small clusters < 1 nm confirmed by PDF and TEM) in strong interaction with the support, as emphasized by TPR and XPS data, which is not straightforward for such a metal when supported on silica (see reference samples prepared by a more conventional impregnation pathway). After reduction, well-distributed Ni^0 NPs were formed with a mean diameter of about 3 nm, which leads to amongst the highest dispersions of Ni (around 30%) reported to date on silica. It is noteworthy that this preparation method remains effective while increasing the metal loading (e.g. $Ni_{7.5\%}$@S has been synthesized and exhibited comparable results to 2.5 and 5 wt.% solids (Ni dispersion: 29%, $S_{BET} \approx 500\ m^2\ g^{-1}$; see also other data in Figure S18)). Better catalytic performances in Dry Reforming of Methane were obtained with these materials. The presence of small Ni particles in strong interaction with silica led also to a remarkably enhanced stability of the samples prepared by the one-pot method with much more limited coke formation and particles aggregation, as demonstrated by the XRD, TGA and TEM data obtained on the $Ni^0_{5\%}$@S spent catalyst. One can expect differences in CH_4 and CO_2 adsorptions behavior on $Ni^0_{5\%}$@S and $Ni^0_{5\%}$/S as function of nickel particle size as already shown by C. Vogt et al [50] but such those investigations would require the use of non-steady-state and steady-state isotopic transient experiments combined with in situ DRIFT spectroscopy investigations.

Acknowledgments

The authors sincerely acknowledge the ERANETMED EU-FP7 initiative, the national ANR (France), CNRS-L (Lebanon) agencies and the Lebanese University for their financial support through the SOL-CARE (Energy-065) project (JC-EN- ERGY-2014 first call) and the French national project METSA for providing them with access to the microscope platform of IPCMS in Strasbourg. The authors would like also to thank Dr C. Louis for fruitful discussions.

Conflicts of interest

The authors have no conflicts of interest to declare.

References

[1] X. Zhao, H. Li, J. Zhang, L. Shi, D. Zhang, Design and synthesis of NiCe@m-SiO_2 yolk-shell framework catalysts with improved coke- and sintering-resistance in dry reforming of methane, Int. J. Hydrogen. Energ. 41 (2016) 2447-2456, https://doi.org/10.1016/j.ijhydene.2015.10.111.

[2] S. Dasa, M. Senguptaa, J. Patel, A. Bordoloi, A study of the synergy between support surface properties and catalyst deactivation for CO_2 reforming over supported Ni nanoparticles, Appl. Catal. A: Gen. 545 (2017) 113-126, https://doi.org/10.1016/j.apcata.2017.07.044.

[3] A. J. Van Dillen, R. J. Terörde, D. J. Lensveld, J. W. Geus, K. P. De Jong, Synthesis of supported catalysts by impregnation and drying using aqueous chelated metal complexes, J. Catal. 216 (2003) 257-264, https://doi.org/10.1016/S0021-9517(02)00130-6.

[4] J.H. Kim, D. J. Suh, T.-J. Park, K.-L. Kim, Effect of metal particle size on coking during CO_2 reforming of CH_4 over Ni–alumina aerogel catalysts, Appl. Catal. A: Gen. 197 (2000) 191-200, https://doi.org/10.1016/S0926-860X(99)00487-1.

[5] B. Abdullah, N. A. Abd Ghani, D.N. Vo, Recent advances in dry reforming of methane over Ni-based catalysts, J. Clean. Prod. 162 (2017) 170-185, https://doi.org/10.1016/j.jclepro.2017.05.176.

[6] E. C. Lovell, A. Fuller, J. Scott, R. Amal, Enhancing Ni-SiO_2 catalysts for the carbon dioxide reforming of methane: Reduction-oxidation-reduction pre-treatment, Appl. Catal. B: Env. 199 (2016) 155-165, https://doi.org/10.1016/j.apcatb.2016.05.080.

[7] J. Woo Han, J. Seong Park, M. Suk Choi, H. Lee, Uncoupling the size and support effects of Ni catalysts for dry reforming of methane, Appl. Catal. B: Env. 203 (2017) 625-632, https://doi.org/10.1016/j.apcatb.2016.10.069.

[8] M. N. Kaydouh, N. El Hassan, A. Davidson, S. Casale, H. El Zakhem, P. Massiani, Highly active and stable Ni/SBA-15 catalysts prepared by a "two solvents" method for dry reforming of methane, Micropor. Mesopor. Mater. 220 (2016) 99-109, https://doi.org/10.1016/j.micromeso.2015.08.034.

[9] D. Pakhare, J. Spivey, A review of dry (CO_2) reforming of methane over noble metal catalysts, Chem. Soc. Rev. 43 (2017) 7813-7837, https://doi.org/10.1039/C3CS60395D.

[10] S. Arora, R. Prasad, An overview on dry reforming of methane: strategies to reduce carbonaceous deactivation of catalysts, RSC Adv. 6 (2016) 108668–108688, https://doi.org/10.1039/C6RA20450C.

[11] S. Kawi, Y. Kathiraser, J. Ni, U. Oemar, Z. Li, Eng Toon Saw, Progress in Synthesis of Highly Active and Stable Nickel-Based Catalysts for Carbon Dioxide Reforming of Methane, ChemSusChem 8 (2015) 3556-3575, https://doi.org/10.1002/cssc.201500390.

[12] E. Baktash, P. Littlewood, J. Pfrommer, R. Schomcker, M. Driess, A. Thomas, Controlled Formation of Nickel Oxide Nanoparticles on Mesoporous Silica using Molecular Ni_4O_4 Clusters as Precursors: Enhanced Catalytic Performance for Dry Reforming of Methane, ChemCatChem 7 (2015) 1280-1284, https://doi.org/10.1002/cctc.201402983.

[13] X. Gao, Z. Tan, K. Hidajat, S. Kawi, Highly reactive Ni-Co/SiO_2 bimetallic catalyst via complexation with oleylamine/oleic acid organic pair for dry reforming of methane, Catal. Today 281 (2017) 250-258, https://doi.org/10.1016/j.cattod.2016.07.013.

[14] C. Wang, X. Jie, Y. Qiu, Y. Zhao, H.A. Al-Megren, S. Alshihri, P.P. Edwards, T. Xiao, The importance of inner cavity space within Ni@SiO_2 nanocapsule catalysts for excellent coking resistance in the high-space-velocity dry reforming of methane, Appl. Catal. B: Env. 259 (2019) 118019, https://doi.org/10.1016/j.apcatb.2019.118019.

[15] J. Xin, H. Cui, Z. Cheng, Z. Zhou, Bimetallic Ni-Co/SBA-15 catalysts prepared by urea co-precipitation for dry reforming of methane, Appl. Catal. A: Gen. 554 (2018) 95-104, https://doi.org/10.1016/j.apcata.2018.01.033

[16] J. Dou, R. Zhang, X. Hao, Z. Bao, T. Wu, B. Wang, F. Yu, Sandwiched SiO_2@Ni@ZrO_2 as a coke resistant nanocatalyst for dry reforming of methane, Appl. Catal. B: Env. 254 (2019) 612-623, https://doi.org/10.1016/j.apcatb.2019.05.021.

[17] N. El Hassan, M. N. Kaydouh, H. Geagea, H. El Zein, K. Jabbour, H. El Zakhem, P. Massiani, Low temperature dry reforming of methane on rhodium and cobalt based catalysts: Active phase stabilization by confinement in mesoporous SBA-15, Appl. Catal. A : Gen. 520 (2016) 114-121, https://doi.org/10.1016/j.apcata.2016.04.014.

[18] C. Wang, Y. Qiu, X. Zhang, Y. Zhang, N. Sun, Y. Zhao, Geometric design of a Ni@silica nano-capsule catalyst with superb methane dry reforming stability: enhanced confinement effect over the nickel site anchoring inside a capsule shell with an appropriate inner cavity, Catal. Sci. Technol., 2018, 8, 4877- 4890, https://doi-org.accesdistant.sorbonne-universite.fr/10.1039/C8CY01158C.

[19] A. Rodriguez-Gomez, R. Pereñiguez, A. Caballero. Nickel Particles Selectively Confined in the Mesoporous Channels of SBA-15 Yielding a Very Stable Catalyst for DRM Reaction, J. Phys. Chem. B 122 (2018) 500-510, https://doi.org/10.1021/acs.jpcb.7b03835.

[20] M. Houalla, F. Delannay, I. Matsuura, B. J. Delmon, Physico-chemical characterisation of impregnated and ion-exchanged silica-supported nickel oxide, J. Chem. Soc. Faraday Trans. 1 76 (1980) 2128-2141, https://doi.org/10.1039/F19807602128.

[21] S. Wu, Y. Han, Y.C. Zou, J.W. Song, L. Zhao, Y. Di, S.Z. Liu, F.S. Xiao, Synthesis of Heteroatom Substituted SBA-15 by the "pH-Adjusting" Method, Chem. Mater. 16 (2004) 486-492, https://doi.org/10.1021/cm0343857.

[22] S. Boujday, J.-F. Lambert, M. Che, Amorphous silica as a versatile supermolecular ligand for Ni^{II} amine Complexes: Toward Interfacial Molecular Recognition, ChemPhysChem 5 (2004) 1003-1013, https://doi.org/10.1002/cphc.200400008.

[23] O. Daoura, S. Daher, M.N. Kaydouh, N. El Hassan, P. Massiani, F. Launay, M. Boutros, Influence of the swelling agents of siliceous mesocellular foams on the performances of Ni-based methane dry reforming catalysts, Int. J. Hydrogen. Energ. 43 (2018) 17205-17215, https://doi.org/10.1016/j.ijhydene.2018.07.123.

[24] O. Daoura, M.N. Kaydouh, N. El Hassan, P. Massiani, F. Launay, M. Boutros, Mesocellular silica foam-based Ni catalysts for dry reforming of CH_4 (by CO_2), J. CO_2 Util. 24 (2018) 112-119, https://doi.org/10.1016/j.jcou.2017.12.010.

[25] E. Delahaye, R. Moulin, M. Aouadi, V. Trannoy, P. Beaunier, G. Fornasieri, A. Bleuzen, Co^{2+}@mesoporous silica monoliths: Tailor-made nanoreactors for confined soft chemistry, Chem. Eur. J. 21 (2015) 16906-16916, https://doi.org/10.1002/chem.201501918.

[26] S. B. Tsai, H. Ma, A research on preparation and application of the monolithic catalyst with interconnecting pore structure, Nature scientific reports, (2018) 8:16605, https://doi.org/10.1038/s41598-018-35021-2.

[27] J. van der Meer, I. Bardez-Giboire, C. Mercier, B. Revel, A. Davidson, R. Denoyel, Mechanism of metal oxide nanoparticle loading in SBA-15 by the double solvent technique, J. Phys. Chem. C 114 (2010) 3507-3515, https://doi.org/10.1021/jp907002y.

[28] P. Juhás, T. Davis, C. L. Farrow, S. J. L. Billinge, PDFgetX3: a rapid and highly automatable program for processing powder diffraction data into total scattering pair distribution functions, J. Appl. Crystallogr. 46 (2013) 560-566, https://doi.org/10.1107/S0021889813005190.

[29] C. L. Farrow, P. Juhas, J. W. Liu, D. Bryndin, E. S. Boin, J. Bloch, T. Proffen, S. J. L. Billinge, PDFfit2 and PDFgui: computer programs for studying nanostructure in crystals, J. Phys. Condens. Matter. 19 (2007) 335219, https://doi.org/10.1088/0953-8984/19/33/335219.

[30] M. Thomme, K. Kaneko, A. V. Neimark, J. P. Olivier, F. Rodriguez-Reinoso, J. Rouquerol, K. S.W. Sing, Physisorption of gases, with special reference to the evaluation of surface area and pore size distribution (IUPAC Technical Report), Pure Appl. Chem. (2015) 1051; aop, http://doi.org/10.1515/pac-2014-1117.

[31] N. Wang, X. Yu, Y. Wang, W. Chu, M. Liu, A comparison study on methane dry reforming with carbon dioxide over $LaNiO_3$ perovskite catalysts supported on mesoporous SBA-15, MCM-41 and silica carrier, Catal. Today 212 (2013) 98-107, https://doi.org/10.1016/j.cattod.2012.07.022.

[32] M. E. Gálvez, A. Albarazi, P. Da Costa, Enhanced catalytic stability through non-conventional synthesis of Ni/SBA-15 for methane dry reforming at low temperatures, Appl. Catal. A: Gen. 504 (2015) 143-150, https://doi.org/10.1016/j.apcata.2014.10.026.

[33] M. J. F. M. Verhaak, A. J. van Dillen, J. W. Geus, Measuring the acid-base properties of supported nickel catalysts using temperature-programmed desorption of ammonia, Appl. Catal. A: Gen. 105 (1993) 251-269, https://doi.org/10.1016/0926-860X(93)80251-K.

[34] M. Che, Z. X. Cheng, C. Louis, Nucleation and particle growth processes involved in the preparation of silica-supported nickel materials by a two-step procedure, J. Am. Chem. Soc. 117 (1995) 2008-2018, https://doi.org/10.1021/ja00112a014.

[35] Z. Bian, S. Kawi, Preparation, characterization and catalytic application of phyllosilicate: A review, Catal. Today 339 (2020) 2-13, https://doi.org/10.1016/j.cattod.2018.12.030.

[36] M.A. Peck, M.A. Langell, Comparison of nanoscaled and bulk NiO structural and environmental characteristics by XRD, XAFS, and XPS, Chem. Mater. 24 (2012) 4483-4490, https://doi.org/10.1021/cm300739y.

[37] K.O. Sebakhy, G. Vitale, P. Pereira-Almao, Production of Highly Dispersed Ni within Nickel Silicate Materials with the MFI Structure for the Selective Hydrogenation of Olefins, Ind. Eng. Chem. Res., 58 (2019) 8597-8611, https://doi.org/10.1021/acs.iecr.8b05991.

[38] Preparation and characterization of a highly dispersed and stable Ni catalyst with a microporous nanosilica support, M. Yang, H. Wu, H. Wu, C. Huang, W. Weng, M. Chen, H. Wan, RSC Adv. 6 (2016) 81237-81244, https://doi.org/10.1039/C6RA15358E.

[39] X. Yan, T. Hu, P. Liu, S. Li, B. Zhao, Q. Zhang, W. Jiao, S. Chen, P. Wang, J. Lu, L. Fan, X. Deng, Y.-X. Pan, Highly efficient and stable Ni/CeO_2-SiO_2 catalyst for dry reforming of methane: Effect of interfacial structure of Ni/CeO_2 on SiO_2, Appl. Catal. B: Env. 246 (2019) 221-231, https://doi.org/10.1016/j.apcatb.2019.01.070.

[40] C. H. Bartholomew, Hydrogen adsorption on supported cobalt, iron, and nickel, Catal. Lett. 7 (1990) 27-51, https://doi.org/10.1007/BF00764490.

[41] J. Wei, E. Iglesia, Isotopic and kinetic assessment of the mechanism of reactions of CH_4 with CO_2 or H_2O to form synthesis gas and carbon on nickel catalysts, J. Catal. 224 (2004) 370-383, https://doi.org/10.1016/j.jcat.2004.02.032.

[42] G. Bergeret, P. Gallezot, Handbook of heterogeneous catalysis, Particle Size and Dispersion Measurements, https://doi.org/10.1002/9783527610044.hetcat0038.

[43] J. Tian, B. Ma, S. Bu, Q. Yuan, C. Zhao, One-pot synthesis of highly sintering- and coking-resistant Ni nanoparticles encapsulated in dendritic mesoporous SiO_2 for methane dry reforming, Chem. Commun. 54 (2018) 13993-13996, https://doi.org/10.1039/C8CC08284G.

[44] C. Chen, X. Wang, L. Zhang, X. Zou, W. Ding, X. Lu, Synthesis of mesoporous Ni-La_2O_3/SiO_2 by poly(ethylene glycol)-assisted sol-gel route as highly efficient catalysts for dry reforming of methane with a H_2/CO ratio of unity, Catal. Commun. 94 (2017) 38-41, https://doi.org/10.1016/j.catcom.2017.02.018.

[45] Y. Zhao, H. Li, H. Li, NiCo@SiO_2 core-shell catalyst with high activity and long lifetime for CO_2 conversion through DRM reaction, Nano Energ. 45 (2018) 101-108, https://doi.org/10.1016/j.nanoen.2017.12.023.

[46] Z. Li, S. Kawi, Multi-Ni@Ni phyllosilicate hollow sphere for CO_2 reforming of CH_4: influence of Ni precursors on structure, sintering, and carbon resistance, Catal. Sci. Technol. 8 (2018) 1915-1922, https://doi.org/10.1039/C8CY00024G.

[47] J. Zhang, F. Li, Coke-resistant Ni@SiO_2 catalyst for dry reforming of methane, Appl. Catal. B: Environ. 176-177 (2015) 513-521, https://doi.org/10.1016/j.apcatb.2015.04.039.

[48] R. J. Zhang, G. F. Xia, M. F. Li, Y.Wu, H. Nie, D. D. Li, Effect of support on the performance of Ni-based catalyst in methane dry reforming, J. Fuel Chem. Technol., 43 (2015) 1359-1365, https://doi.org/10.1016/S1872-5813(15)30040-2.

[49] Q. Liu,Y. Tian, One-pot synthesis of NiO/SBA-15 monolith catalyst with a three-dimensional framework for CO_2 methanation, International Journal of Hydrogen Energy, 42 (2017) 12295-12300, https://doi.org/10.1016/j.ijhydene.2017.02.070.

[50] C. Vogt, J. Kranenborg, M. Monai, B.M. Weckhuysen, Structure Sensitivity in Steam and Dry Methane Reforming over Nickel: Activity and Carbon Formation, ACS Catal., 10 (2020) 1428-1438, https://doi.org/10.1021/acscatal.9b04193.

Figure captions

Figure 1: A: N_2 adsorption-desorption isotherms at -196°C and pores size distributions. B: Small angles XRD patterns of the calcined samples: S (black), $Ni^{II}_{5\%}$/S (purple) and $Ni^{II}_{5\%}$@S (red, sample prepared using the one-pot synthesis).

Figure 2: H_2-TPR profiles of the calcined $Ni^{II}_{5\%}$-S samples recorded with a H_2 5 vol.%/Ar flow of 30 mL min^{-1} and a heating rate of 10°C min^{-1}.

Figure 3: XP Spectra of the calcined $Ni^{II}_{5\%}$@S and $Ni^{II}_{5\%}$/S samples.

Figure 4: TEM images of microtomed $Ni^{II}_{5\%}$/S (A, A', B) and $Ni^{II}_{5\%}$@S (D, E and F) in their calcined state. HR-TEM image and SAED patterns of $Ni^{II}_{5\%}$/S (C).

Figure 5: PDF analysis – A) Simulated G(r) curve (typical signature) for NiO (in blue) and Ni^0 (in Green) and B) Normalized experimental G(r) of $Ni^{II}_{5\%}$@S (in red) compared to normalized G(r) of silica support without nickel (in Blue). Red stars emphasize the 3 higher intensities at 2.1, 3.1 and 5.3 Å related to NiO structure.

Figure 6: STEM/HAADF and EDX/mapping (with Ni in green, Si in yellow and O in purple) acquired with two different magnifications on typical areas of the calcined microtomed $Ni^{II}_{5\%}$@S sample.

Figure 7: Typical TEM images of reduced microtomed $Ni^0_{5\%}$/S (A, A', B) and $Ni^0_{5\%}$@S (C, D) samples.

Figure 8: A) Representative 2D STEM-HAADF image of $Ni_{5\%}$@S sample extracted from the tilt series used to calculate the 3D reconstruction of the chosen aggregate, with the corresponding STEM Bright Field image in inset. The white contrasted spots in the image correspond to gold nanoparticles deposited on the TEM membrane after the deposition of the specimen, to be used as fiducial markers for the alignment of the images of the tilt series before the reconstruction ; B) Three orthogonal views through the volume of the catalyst nanograin obtained by electron tomography ; C) Typical slice extracted from the reconstruction corresponding to the area highlighted by a red square in A ; D) The corresponding 3D model of the same area.

Figure 9: CH_4 and CO_2 conversions, and H_2/CO molar ratio in the DRM reaction on $Ni^0_{5\%}$@S. A: as a function of temperature and B: as a function of time on steam at 650°C under a GHSV of 144 L g^{-1} h^{-1}.

Figure 10: A: CH_4 and CO_2 conversions, and B: H_2/CO molar ratio in the DRM reaction on $Ni^0_{5\%}$/S (Purple) and $Ni^0_{5\%}$@S (red) at 650°C during 12 h on steam under a GHSV of 960 L g^{-1} h^{-1}.

Figure 1

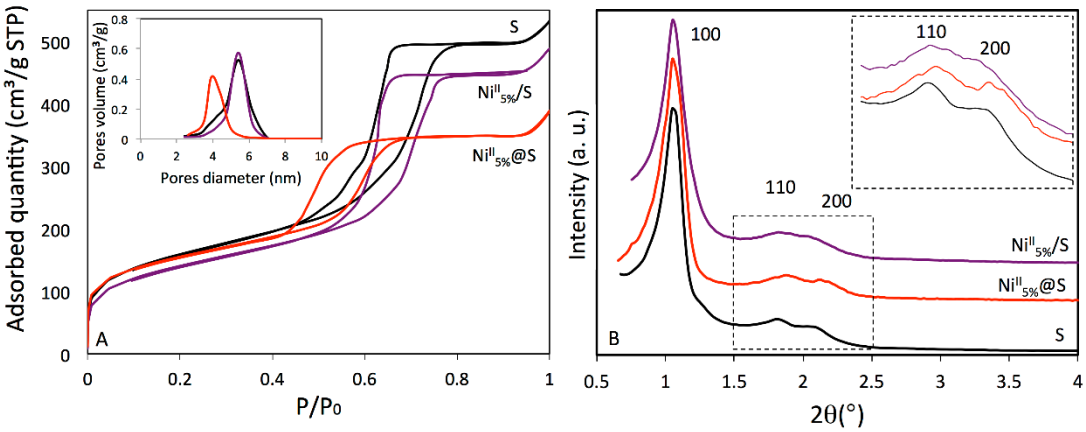
Adsorbed quantity (cm³/g STP)
P/P0
Pores volume (cm³/g)
Pores diameter (nm)
S
Ni$^{II}_{5\%}$/S
Ni$^{II}_{5\%}$@S
A
Intensity (a. u.)
2θ(°)
100
110
200
B

Figure 2

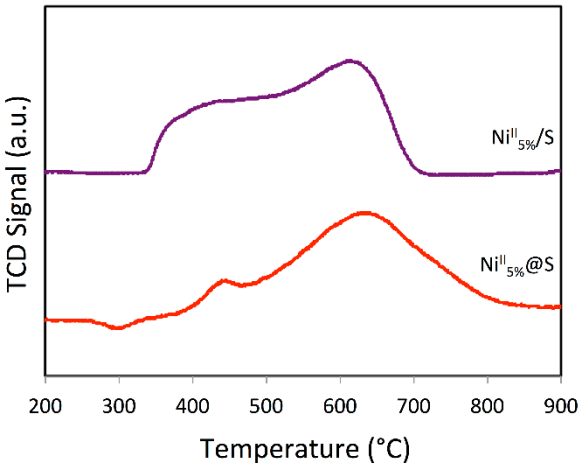
TCD Signal (a.u.)
Ni$^{II}_{5\%}$/S
Ni$^{II}_{5\%}$@S
200
300
400
500
600
700
800
900
Temperature (°C)

Figure 3

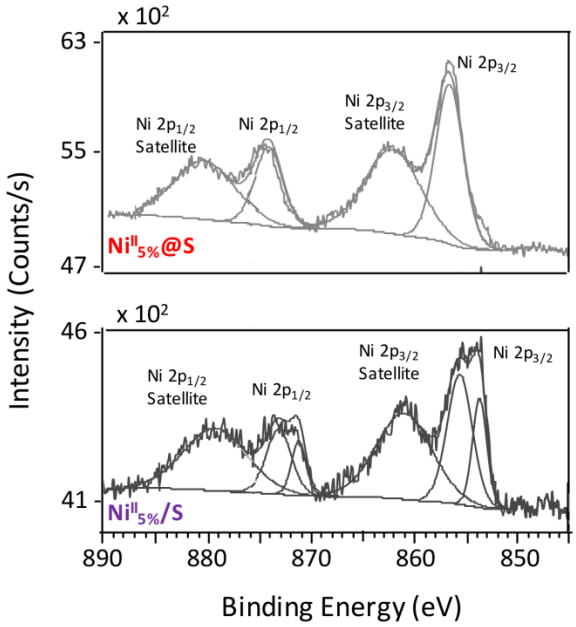
x 10²
63
55
47
Ni 2p3/2
Ni 2p3/2 Satellite
Ni 2p1/2
Ni 2p1/2 Satellite
Niᴵᴵ5%@S
x 10²
46
41
Ni 2p3/2
Ni 2p3/2 Satellite
Ni 2p1/2
Ni 2p1/2 Satellite
Niᴵᴵ5%/S
Intensity (Counts/s)
890
880
870
860
850
Binding Energy (eV)

Figure 4

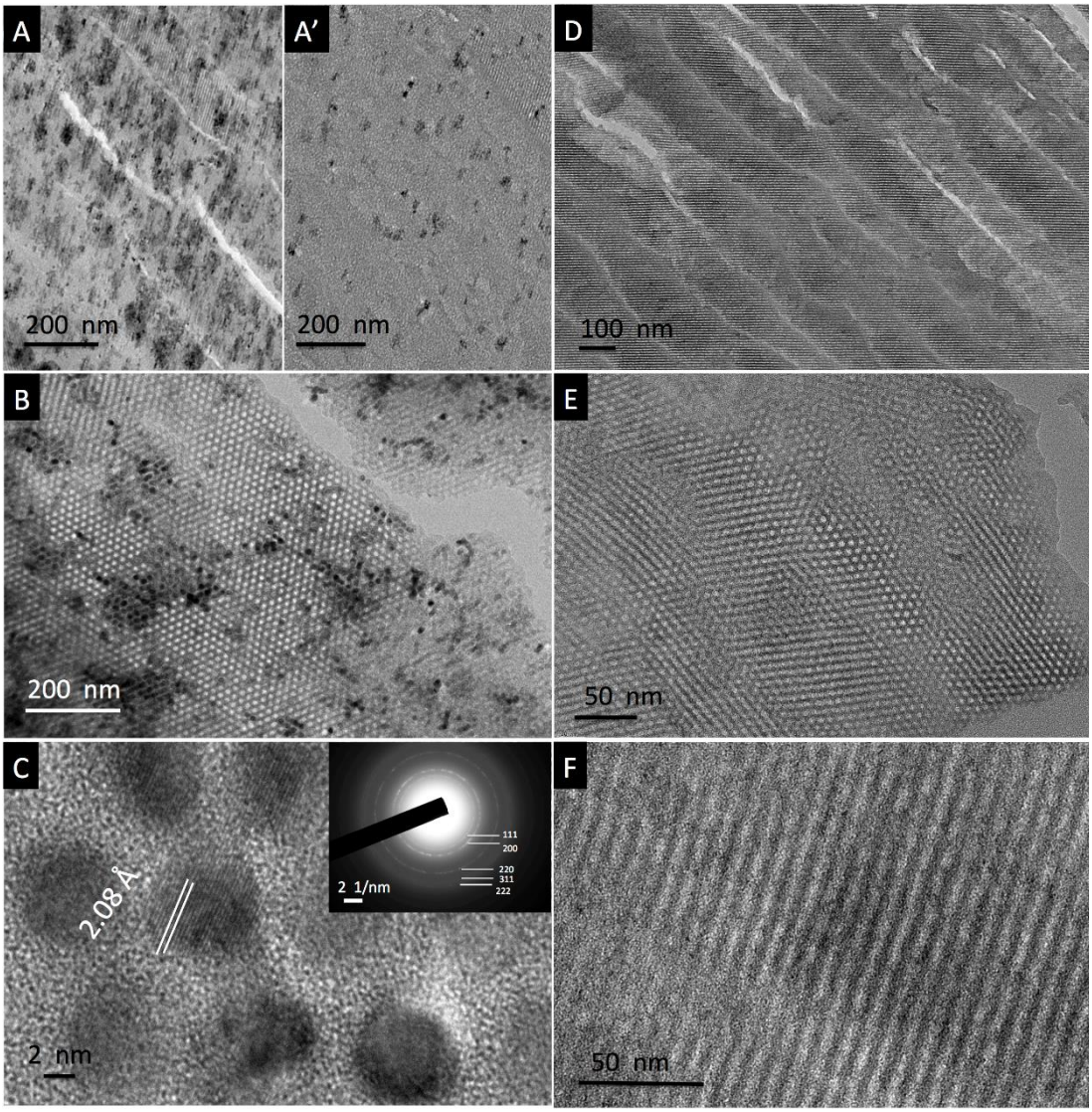
A
200 nm
A'
200 nm
D
100 nm
B
200 nm
E
50 nm
C
2.08 Å
2 nm
2 1/nm
111
200
220
311
222
F
50 nm

Figure 5

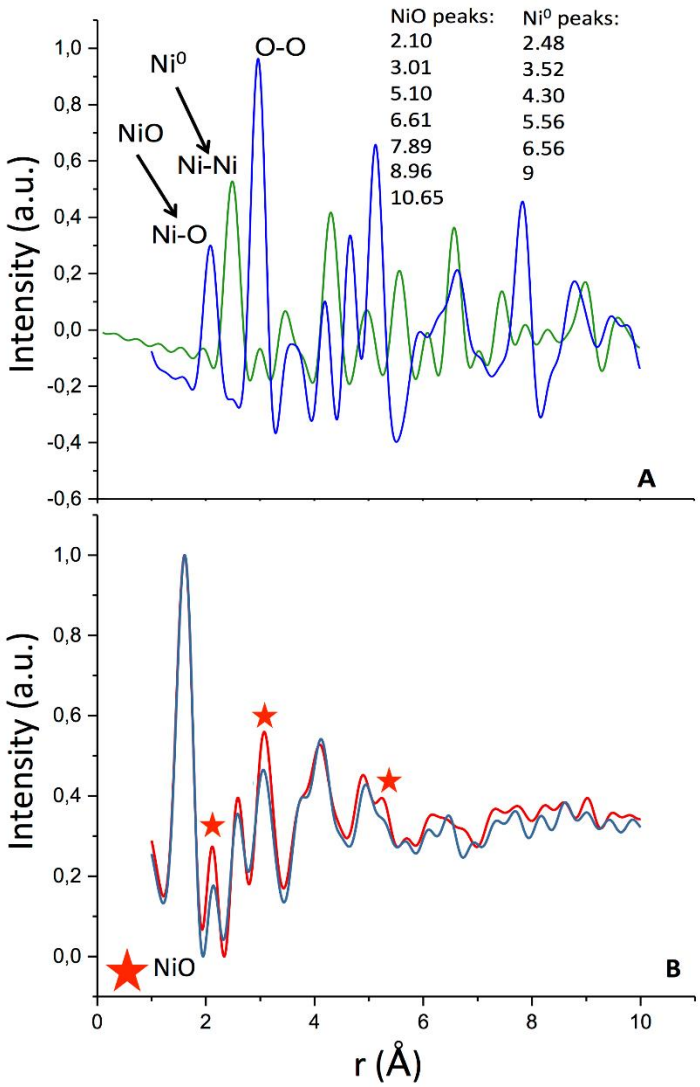
NiO peaks:
2.10
3.01
5.10
6.61
7.89
8.96
10.65
Ni⁰ peaks:
2.48
3.52
4.30
5.56
6.56
9
Ni⁰
O-O
NiO
Ni-Ni
Ni-O
Intensity (a.u.)
A
B
NiO
r (Å)

Figure 6

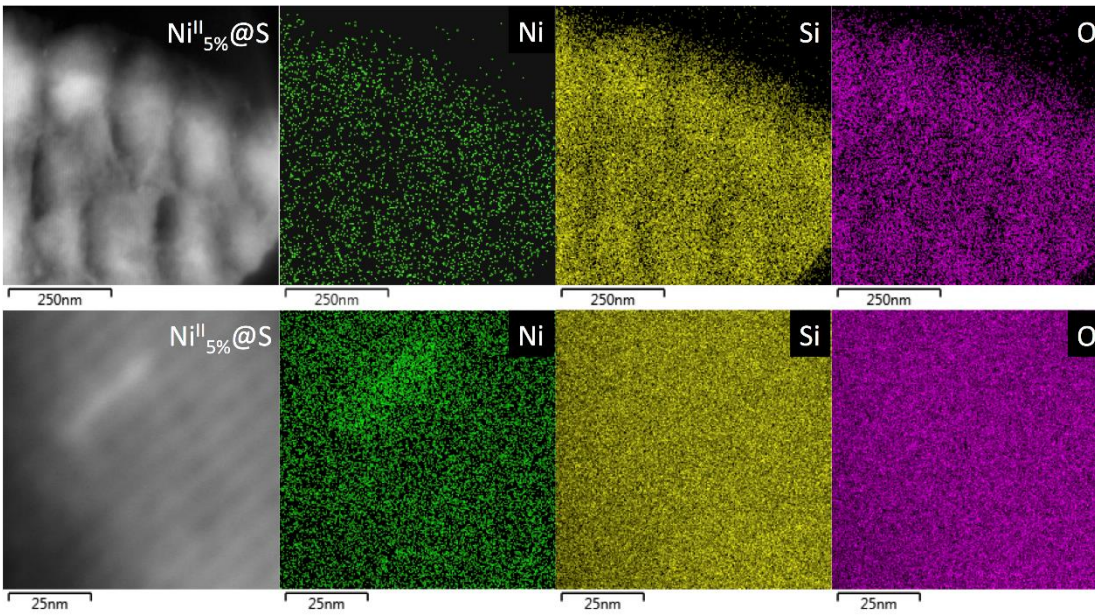
Ni$^{II}_{5\%}$@S
Ni
Si
O
250nm
250nm
250nm
250nm
Ni$^{II}_{5\%}$@S
Ni
Si
O
25nm
25nm
25nm
25nm

Figure 7

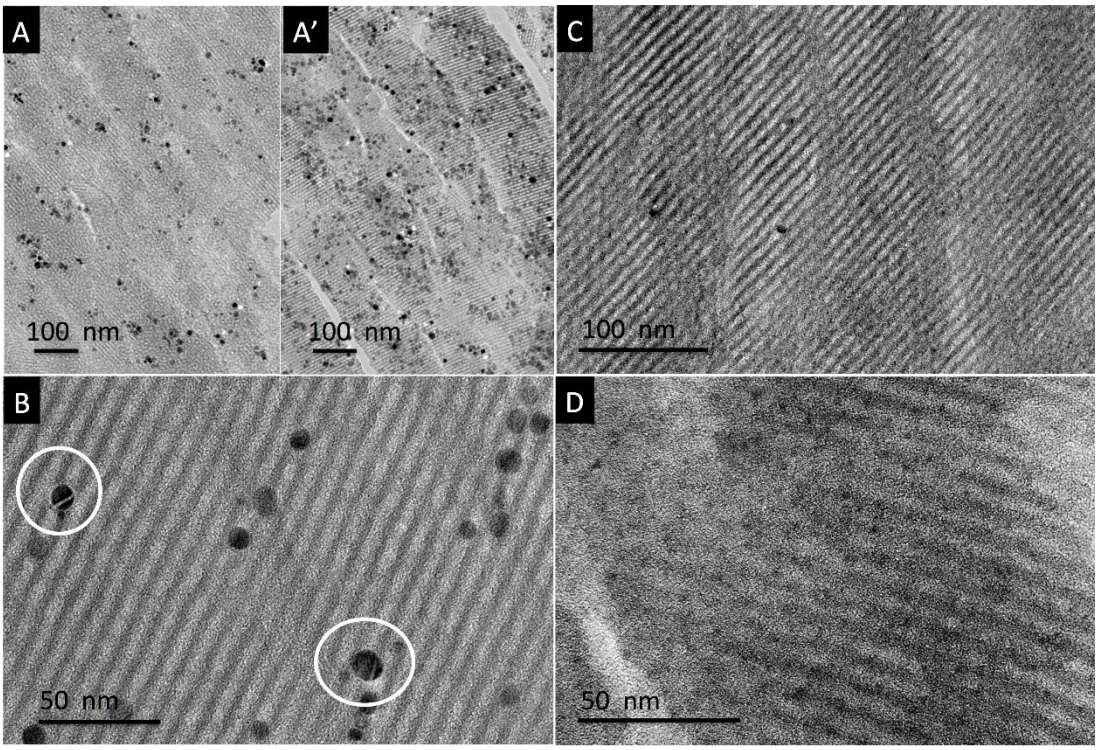

Figure 8

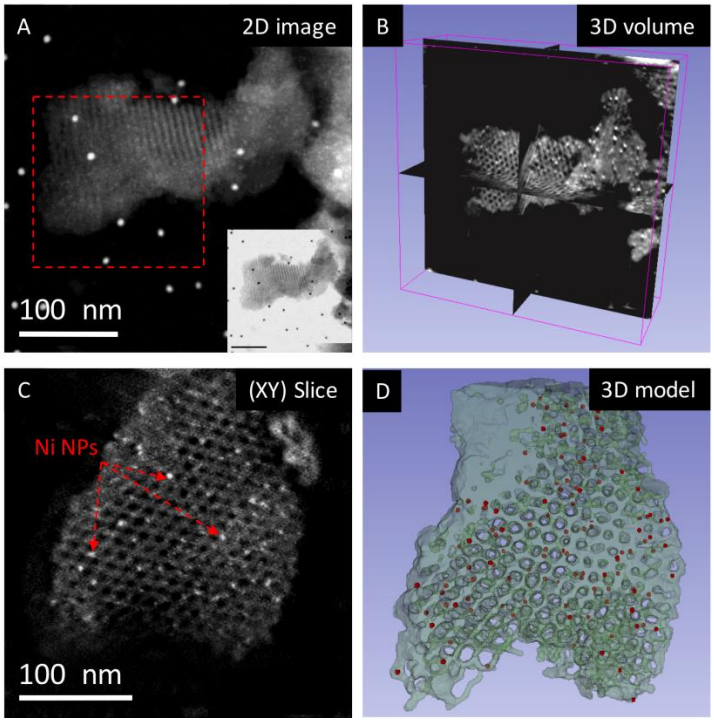

Figure 9

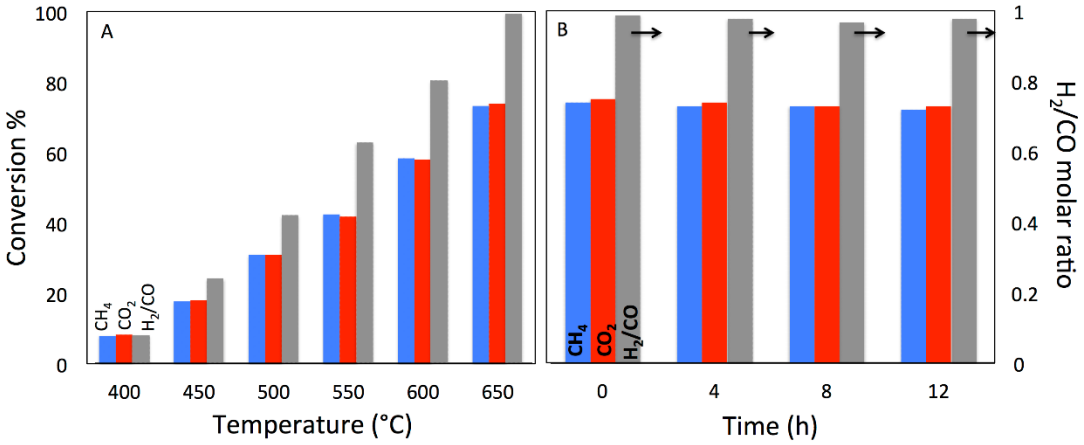
A
B
Conversion %
100
80
60
40
20
0
CH4
CO2
H2/CO
400
450
500
550
600
650
Temperature (°C)
0
4
8
12
Time (h)
1
0.8
0.6
0.4
0.2
0
H2/CO molar ratio

Figure 10

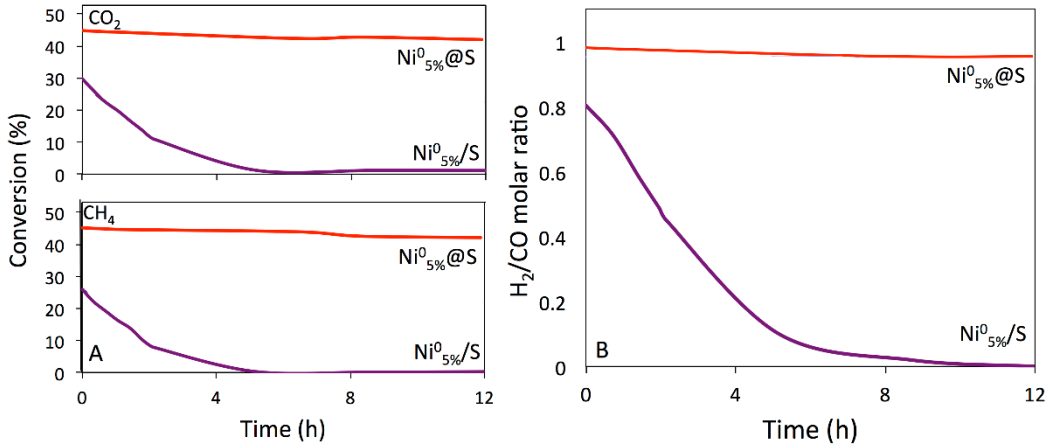
CO2
Ni0 5%@S
Ni0 5%/S
CH4
Ni0 5%@S
Ni0 5%/S
A
Conversion (%)
Time (h)
Ni0 5%@S
Ni0 5%/S
B
H2/CO molar ratio
Time (h)

List of tables

Table 1: *Physicochemical properties of the calcined Ni-SBA-15 monolith samples.*

Samples	Calcined					Reduced
	Ni [a] **(wt. %)**	**S_{BET} (m^2 g^{-1})**	**V_{Des}** [b] **(cm^3 g^{-1})**	**D_{pores}** [c] **(nm)**	**NiO size** [d] **(nm)**	**Ni^0 size** [e] **(nm)**
Support S	---	574	0.81	5.4	-	-
$Ni^{II}_{2.5\%}$/S	1.7	519	0.77	5.4	5.3	-
$Ni^{II}_{5\%}$/S	6.8	507	0.75	5.4	5.4	8.0
$Ni^{II}_{2.5\%}$@S	2.0	570	0.65	4.2	n.d.[f]	-
$Ni^{II}_{5\%}$@S	4.5	562	0.55	4.0	n.d.[f]	2.1

[a] Estimated from the H_2 consumptions during the TPR measurements (good agreement between the Ni contents determined by H_2-TPR (4.5 wt.%) and by ICP-EOS analysis (4.2 wt.%) for $Ni^{II}_{5\%}$@S); [b] Estimated from BJH on the desorption branch; [c] Deduced from the BJH desorption pore size distribution; [d] and [e] From TEM images after measuring about 400 particles; [f] not detected.

Table 2: *H_2 chemisorption data recorded at 25°C after reduction under H_2 at 650°C for 2 h and evacuation at 620°C for 1 h, Ni dispersion and TOF in the DRM reaction.*

Materials	**Amount of H_2 chemisorbed ($cm^3\ g^{-1}$)**	**Ni dispersion (%)**	**Ni particle diameter [a] (nm)**	**TOF [b] (s^{-1}) initial**	**TOF [b] (s^{-1}) After 12 h on stream**
$Ni^0_{5\%}$/S	1.04	8.0	12.6	1.7	~ 0
$Ni^0_{5\%}$@S	2.66	31.0	3.3	1.2	1.1
$Ni^0_{2.5\%}$@S	1.35	35.0	2.9	1.4	1.2

[a] From H_2 chemisorption; [b] CH_4 TOF at 650 °C (see Supporting information section).

One-pot prepared mesoporous silica SBA-15-like monoliths with embedded Ni particles as selective and stable catalysts for methane dry reforming

Oscar Daoura[a,b], Giulia Fornasieri[c], Maya Boutros[a], Nissrine El Hassan[d], Patricia Beaunier[b], Cyril Thomas[b], Mohamed Selmane[e], Antoine Miche[b], Capucine Sassoye[f], Ovidiu Ersen[g], Walid Baaziz[g], Pascale Massiani[b], Anne Bleuzen[c]* and Franck Launay[b]*

[a] Laboratoire de Chimie Physique des Matériaux (LCPM/PR2N), Lebanese University, Faculté des Sciences II, Campus Fanar, BP 90696 Jdeideh, Lebanon.

[b] Laboratoire de Réactivité de Surface (LRS), UMR 7197 CNRS - Sorbonne Université, Campus Pierre et Marie Curie, 4 place Jussieu, F-75005 Paris, France. *franck.launay@sorbonne-universite.fr*

[c] Institut de Chimie Moléculaire et des Matériaux d'Orsay (ICMMO), UMR 8182 CNRS - Université Paris-Saclay, F-91405 Orsay, France. *anne.bleuzen@u-psud.fr*

[d] University of Balamand, Department of Chemical Engineering, P.O. box 33, Amioun El Koura, Lebanon.

[e] Institut des Matériaux de Paris Centre (IMPC), FR 2482 CNRS - Sorbonne Université, Campus Pierre et Marie Curie, 4 place Jussieu, F-75005 Paris, France

[f] Laboratoire de Chimie de la Matière Condensée de Paris (LCMCP), UMR 7574 CNRS - Sorbonne Université, Campus Pierre et Marie Curie, 4 place Jussieu, F-75005 Paris, France.

[g] Institut de Physique et de Chimie des Matériaux de Strasbourg (IPCMS), UMR 7504 CNRS - Université de Strasbourg, 23 rue de Loess, BP43, 67034 Strasbourg Cedex 2, France.

Supporting information

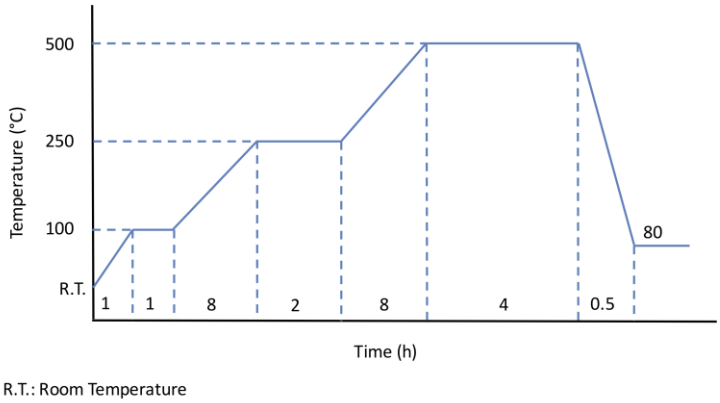

***Figure S1**: Temperature program used for the removal of the organic surfactant (Pluronic P123) during the calcination treatment.*

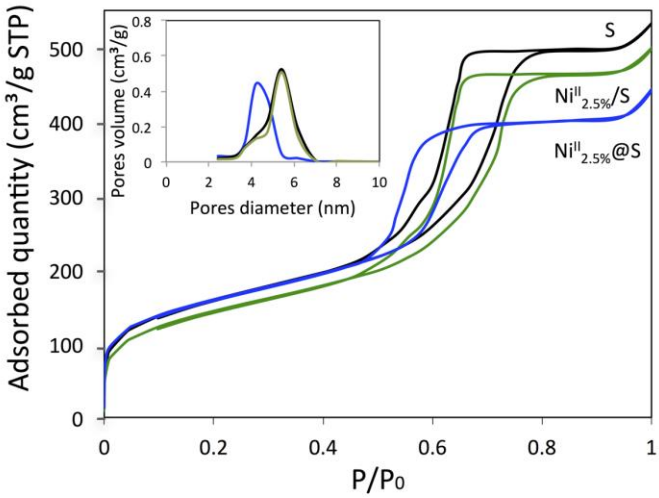

***Figure S2:** N_2 adsorption-desorption isotherms at -196 °C and pores size distributions of the calcined samples: S (black), $Ni^{II}_{2.5\%}$/S (green) and $Ni^{II}_{2.5\%}$@S (blue, prepared using the one-pot strategy).*

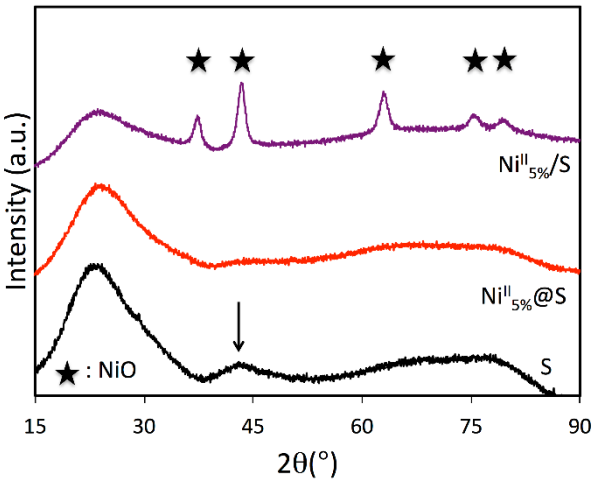

***Figure S3:** Wide angles XRD patterns of calcined $Ni^{II}_{5\%}$/S, $Ni^{II}_{5\%}$@S and of the support, S. The wide peak between 2θ = 15-30° is attributed to diffusion effects by the amorphous silica walls, whereas the wide peak at 42° in the S sample is attributed to the contribution of the PMMA sample holder.*

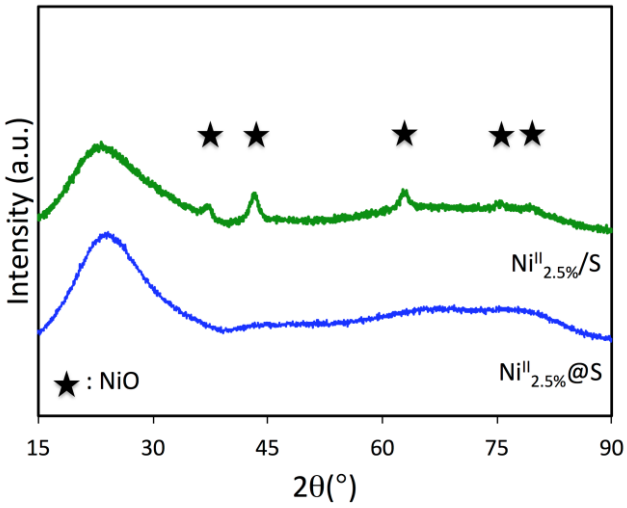

Figure S4: *Wide angles XRD patterns of calcined Ni$^{II}_{2.5\%}$-S samples. The wide peak between 2θ°= 15-30° is attributed to diffusion effects by the amorphous silica walls.*

Figure S4 showed five intense diffraction peaks at 2θ° = 37.2, 43.3, 62.9, 75.4 and 77° for Ni$^{II}_{2.5\%}$/S (particles around 6 nm), whereas its counterpart prepared by the one-pot method (Ni$^{II}_{2.5\%}$@S) did not show any diffraction peak.

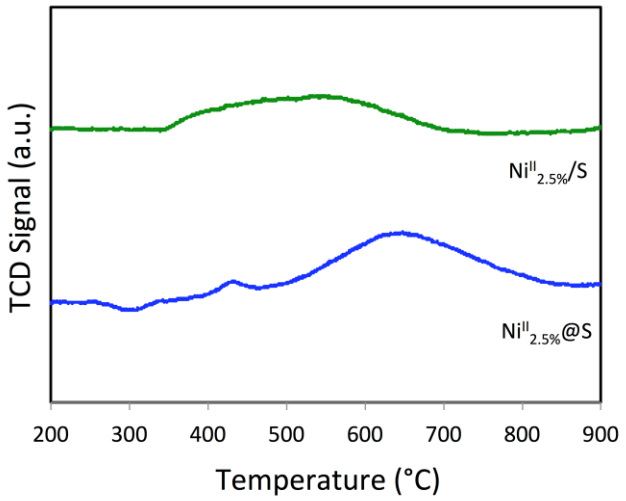

Figure S5: *H_2-TPR profiles of the calcined Ni$^{II}_{2.5\%}$-S samples recorded with a H_2 5 vol.%/Ar flow of 30 mL min^{-1} and a heating rate of 10°C min^{-1}.*

Table S1: *Comparison of the Nickel reducibility behavior for relevant Ni-SiO_2 based catalysts (no phyllosilicates and promoters)*

Preparation method	Solids type	Comments	H_2-TPR Conditions	Ref.
One-Pot	5 wt. % Ni on SBA-15 Monoliths	- **One main peak at 650°C with reduction up to 800°C**	(5 vol% H_2/Ar) Flow: 25 mL min^{-1} Ramping rate 10°C min^{-1}	This work
	15 wt. % on SBA-15	- One main peak at **350°C** (very low probably due to large particles size (17 nm)). - The reduction continues **up to 650°C** (low quantity).	Not mentioned	**[1]**
Impregnation	5 to 10 wt.% of nickel on SBA-15, SBA-16 or mesoporous SiO_2	- Whatever the impregnation method, two reduction peaks were obtained: - First one around **300-450°C** and a second one between **500-650°C**. - some exceptions could be observed when the impregnation was promoted with oleylamine (OAm) and/or oleic acid [5] - By far, no Ni reduction at higher temperature than 750-800°C could be identified.	(5 vol% H_2/Ar or N_2) Flow between 20 to 60 mL min^{-1} Ramping rate 10°C min^{-1}	**[2-5]**
Core-shell (encapsulation)	5 wt.% Nickel in microporous Silica giving cores@Shell structure	-Encapsulated Ni particles within porous SiO_2 (M-Ni@SiO_2 in black) showed **two reduction peaks as well**. - The second peak has shown high reduction temperatures (**around 750°C**)	Not mentionned	**[6]**
Pre-controlled Colloidal particles	0.16 to 0.32 wt.% Ni colloids (different sizes) on silica spheres	One reduction peak perhaps due to the homogeneity of the particles size. It's noteworthy that the higher reduction temperature corresponds to the smaller particles (peak at **420°C**)	(5 vol% H_2/Ar) Ramping rate of 10°C min	**[7]**

<u>According to Table S1, our one-pot preparation method leads to one of the highest metal support interactions obtained in the absence of promoters or for methods which does not involve phyllosilicates as well as to a particles size control (one main reduction peak).</u>

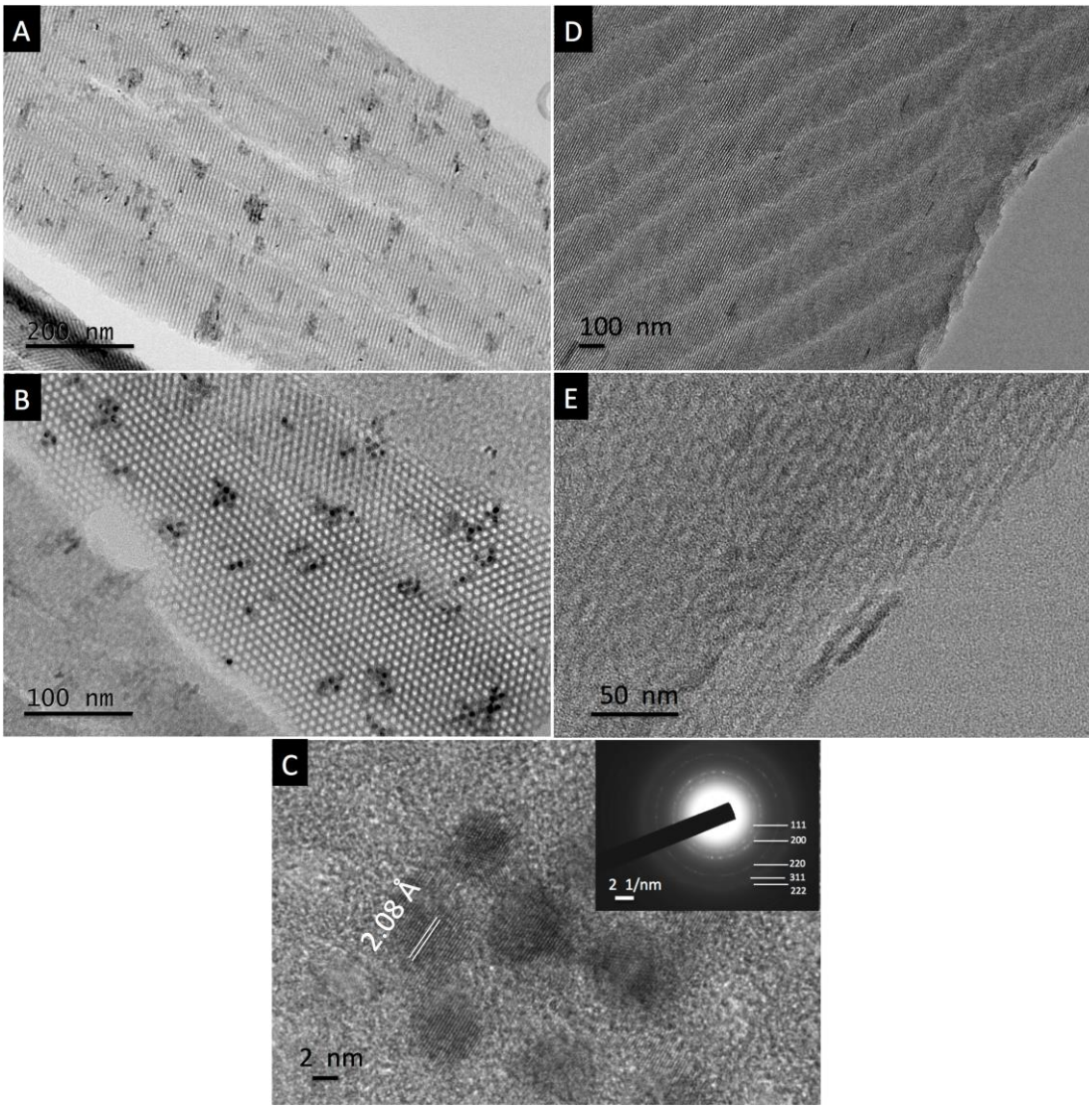

Figure S6: *TEM images of microtomed $Ni^{II}_{2.5\%}$/S (A, B) and $Ni^{II}_{2.5\%}$@S (D and E) in their calcined state. HR-TEM image and SEAD patterns of $Ni^{II}_{2.5\%}$/S (C).*

- $Ni^{II}_{2.5\%}$/S and $\underline{Ni^{II}_{2.5\%}@S}$ exhibited hexagonal mesoporosity (Fig. S6 A, B, D and E).
- In the case of $Ni^{II}_{2.5\%}$/S:
    - Heterogeneously dispersed NiO particles were clearly observed
    - SAED patterns showed five rings which indicates the presence of polycrystalline NiO nanoparticles.
- In the case of $\underline{Ni^{II}_{2.5\%}@S}$, no NiO particle were observed.

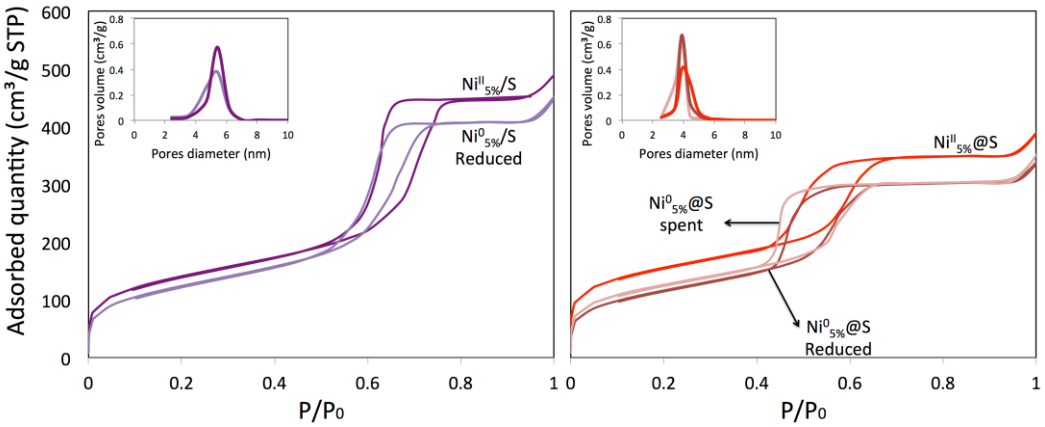

Figure S7: *N_2 sorption isotherms at -196°C and pores size distributions of selected reduced and spent Ni/S and Ni@S (with 5 wt. % Ni) samples.*

Table S2: *Physicochemical properties of the reduced and spent materials.*

Materials	S_{BET} ($m^2\ g^{-1}$)	V_{Pores}[a] ($cm^3\ g^{-1}$)	D[b] (nm)	Ni^0 size [c] (nm)
$Ni^{II}_{5\%}$@S Calcined	562	0.55	4.0	-
$Ni^0_{5\%}$@S Reduced	421	0.53	4.0	2.1
$Ni^0_{5\%}$@S Spent	458	0.53	4.0	2.7
$Ni^{II}_{5\%}$/S Calcined	507	0.75	5.4	-
$Ni^0_{5\%}$/S Reduced	422	0.72	5.4	8.0

[a] From BJH desorption; [b] Average pore diameters deduced from the BJH method applied to the desorption isotherms; [c] Estimated from TEM images after measuring around 400 particles.

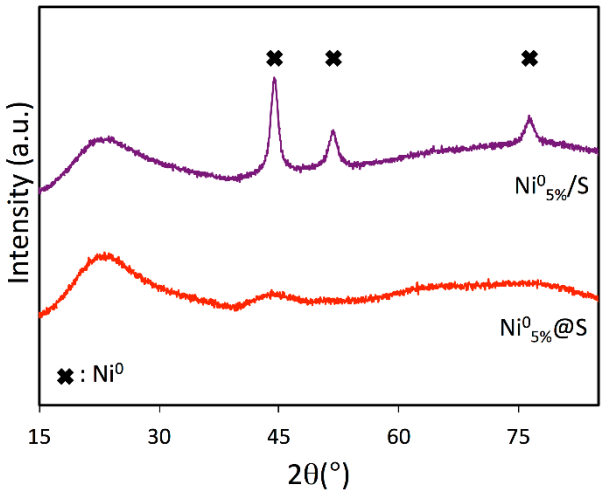

Figure S8: *Wide angles XRD diffraction patterns of the $Ni^0_{5\%}$-S samples (reduced at 650°C for 2 h under a flow of 30 mL min^{-1} of 5 vol.% H_2/Ar). The wide peak between 2θ = 15-30° is assigned to the diffusion effects by the amorphous silica walls.*

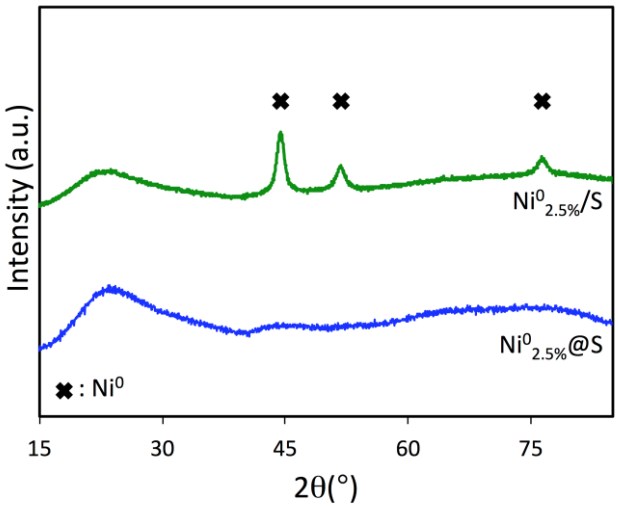

***Figure S9**: Wide angle XRD diffraction patterns of the $Ni^0_{2.5\%}$-S samples (reduced at 650°C for 2 h under a flow of 30 mL min^{-1} of 5 vol.% H_2/Ar). The wide peak between 2 θ = 15–30° is due to diffusion effects by the amorphous silica walls.*

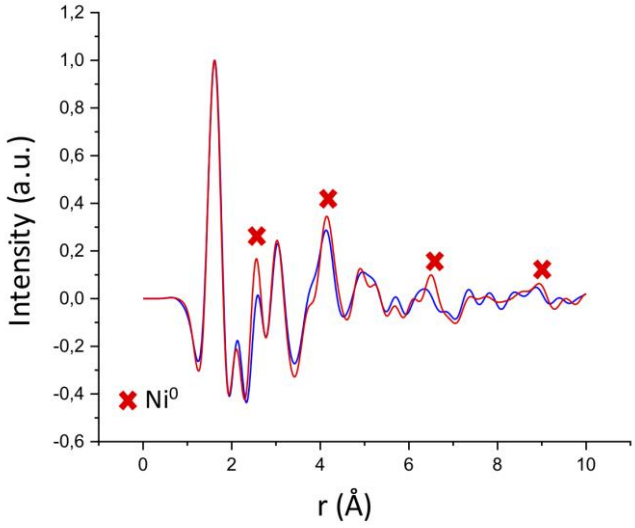

***Figure S10**: PDF analysis: Normalized experimental G(r) of reduced Ni5%@S (in red) compared to normalized S G(r) without nickel (in blue).*

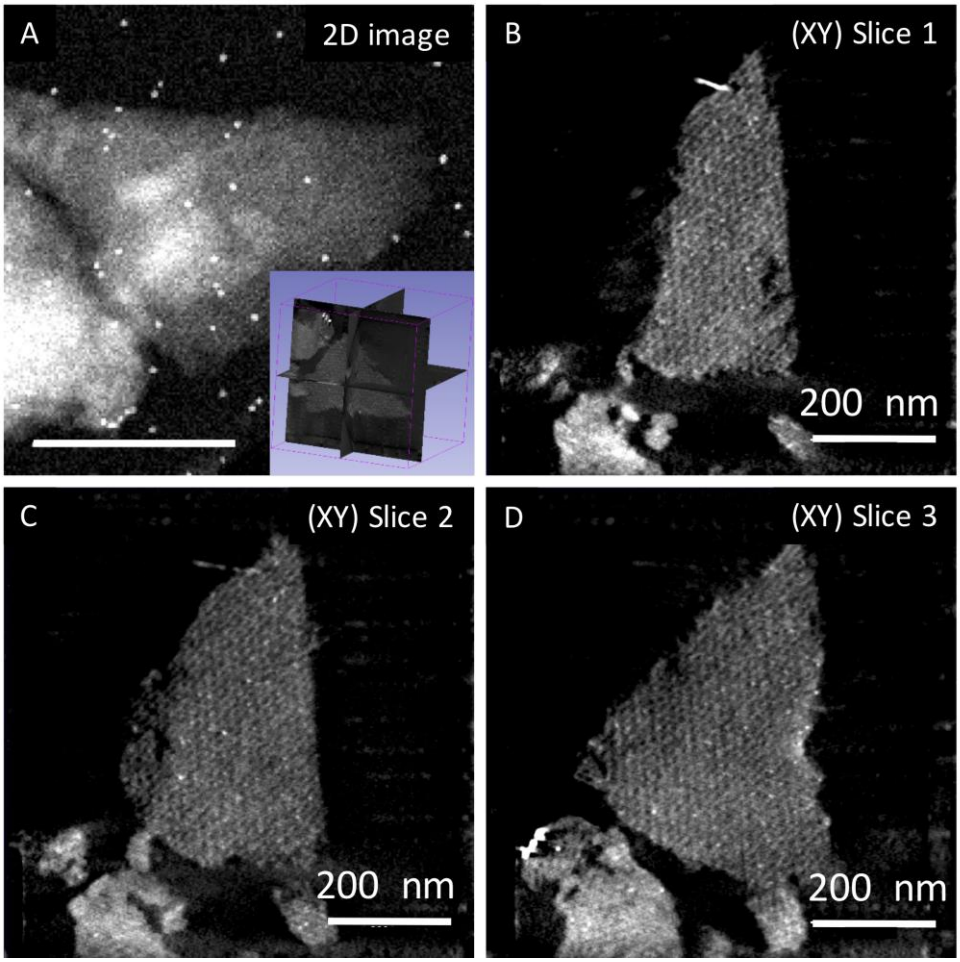

Figure S11*: A) 2D STEM-HAADF image, at 0° tilt, of a second typical grain of $Ni_{5\%}$@S sample chosen for the tomography analysis; this image is extracted from the tilt series used to calculate the 3D reconstruction. The white contrasted spots in the image correspond to gold nanoparticles deposited on the TEM membrane after the deposition of the specimen, to be used as fiducial markers for the alignment of the images of the tilt series before the reconstruction. The corresponding orthogonal views of the calculated reconstruction is shown in inset. B, C and D) Three typical slices extracted from the reconstruction, at different depths, showing the presence of Ni NPs in the whole volume of the mesoporous silica grain and their very good dispersion.*

Table S3: *Ni dispersion on siliceous supports for catalysts used in the DRM reaction reported in earlier works.*

Ref	Authors	Ni (wt.%)	Dispersion (D, %)	Support	Method for D% calculation	Ref[a]
[8]	Qian *et al.*	0.5	40.3	KIT	H_2 chemisorption	-
[9]	Gao *et al.*	5.0	27.1	Mesoporous SiO_2	N_2O pulse titration	-
[5]	Gao *et al.*	5.0	21.0	Mesoporous SiO_2	H_2 chemisorption	-
[10]	Taherian *et al.*	10.0	13.8	SBA-15	TEM	-
[11]	Wang *et al.*	5.0-12.0	11.4	SiO_2 nanocapsule	H_2 chemisorption	-
[2]	Galvez *et al.*	8.0	8.7	SBA-15	H_2 chemisorption	**[31]**
[12]	Wang *et al.*	4.0-8.0	6.8	HMS	CO chemisorption	-

[13]	Li *et al.*	25.0	3.7	SiO_2 nanotubes	H_2 chemisorption	-
[14]	Li *et al.*	10.0	2.0	SBA-15	H_2 chemisorption	-
[15]	Yan *et al.*	5.0	12	SiO_2-CeO_2	CO chemisorption	**[38]**
[16]	Cao *et al.*	5.3	9.7	Ni/BN@mSiO_2	H_2 chemisorption	-

[a] Reference number in the manuscript.

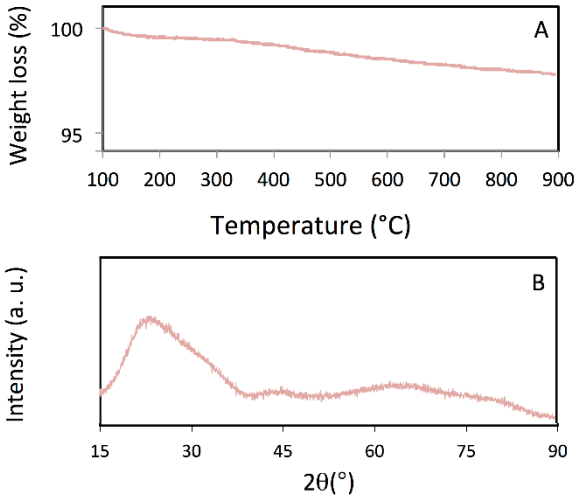

Figure S12: *A: TGA profile and B: XRD pattern of the spent $Ni^0_{5\%}$@S. (The wide peak at 15 < 2θ < 30° in B can be assigned to X-Ray diffusion by the amorphous silica walls).*

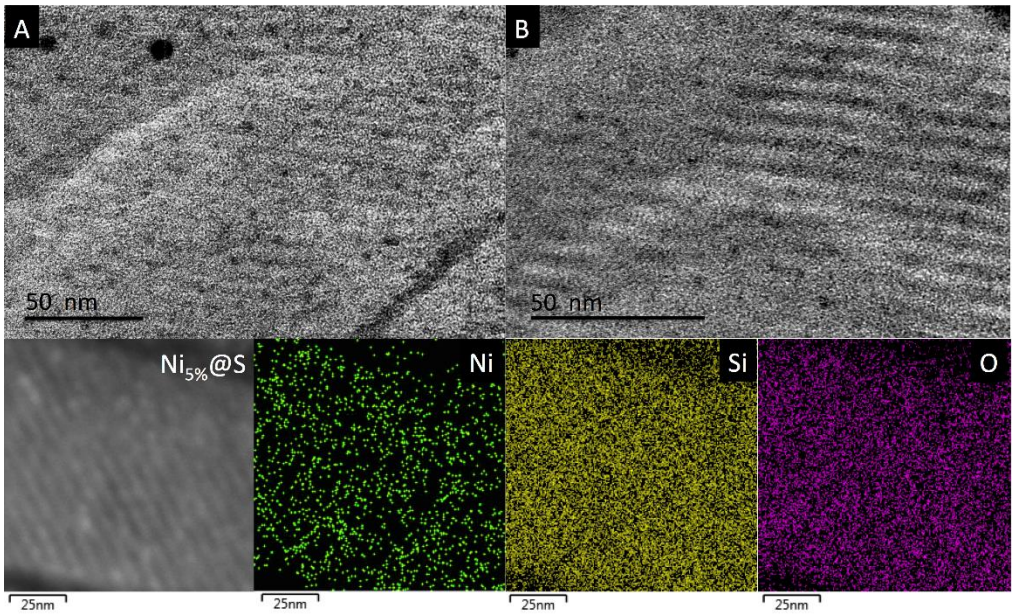

Figure S13: *A and B: TEM images, STEM/HAADF and EDX/mapping (Ni in Green, Si in yellow and O in purple) acquired on typical areas of microtomed spent $Ni^0_{5\%}$@S (GHSV = 144 L g^{-1} h^{-1}).*

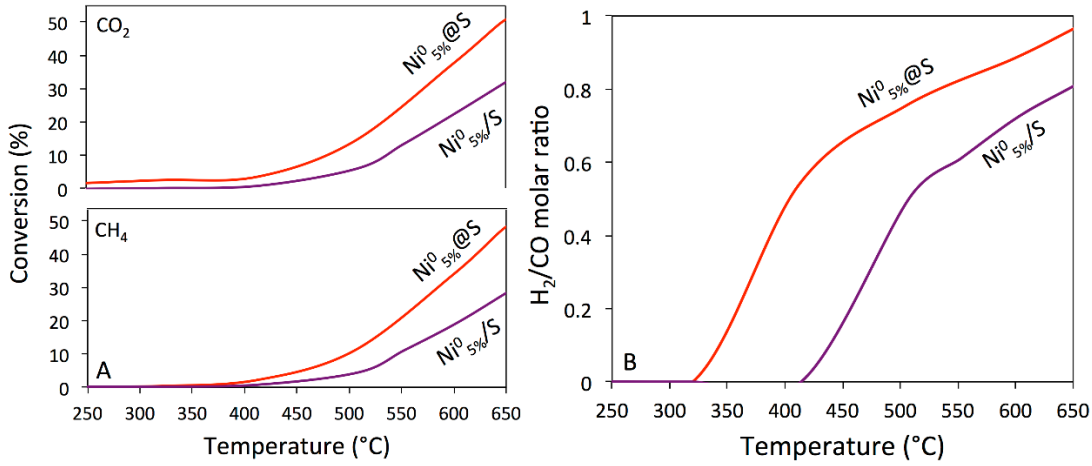

Figure S14: *A: CH_4 and CO_2 conversions, and B: H_2/CO molar ratio in the DRM reaction on $Ni^0_{5\%}$/S (purple) and $Ni^0_{5\%}$@S (red) at 650°C as a function of time on stream under a GHSV of 960 L g^{-1} h^{-1}.*

Table S4: *Detailed experimental parameters of selected studies using Nickel onto silica.*

Ref	Catalyst description	TOF [a] (s^{-1})	T [b] (°C)	GHSV (L g^{-1} h^{-1})	Ni (wt.%)	D_{Ni} [c] (%)	Method	Feed	CH_4 [d] (%)	Ref [e]
[7]	Ni^0 colloids prepared in organic medium deposited onto SiO_2 spheres	61.7	800	12	0.21	n.a.	CO chemisorption	CH_4, CO_2, and N_2 9, 9, and 2 mL min^{-1}	39	**[7]**
[17]	Core-shell Ni@SiO_2	33.4	750	48	29	n.a.	CO chemisorption	CO_2:CH_4 = 1:1 20 mL STP min^{-1}	57	**[47]**
[18]	Multi-Ni@Ni phyllosilicate hollow sphere	12.0	700	1880	40	2	H_2 chemisorption	CO_2:CH_4:He = 1:1:1 314 mL min^{-1}	16	**[46]**
[19]	NiCe@mesoporous SiO_2 core-shell	6.2	500	108	10	3	H_2 chemisorption	CO_2:CH_4 = 1:1 45 mL min^{-1}	n.a.	**[1]**
[5]	Ni/SiO_2 prepared by impregnation assisted with oleylamine	2.8	700	1440	5	21	H_2 chemisorption	CO_2:CH_4:N_2 = 1:1:1 240 mL min^{-1}	8	-
[20]	Ni-3La_2O_3/SiO_2	1.9	700	1440	17.5	n.a.	XRD	CO_2:CH_4 = 1:1	10	**[44]**
[21]	Ni-carbon composites on silica	1.3	550	24	9	n.a.	CO chemisorption	CO_2:CH_4 = 1:1 40 mL min^{-1}	10	-
[22]	Ni nanoparticles in cerium-modified silica aerogels	0.6	500	12	5	10	H_2 chemisorption	CO_2:CH_4 = 1:1 45 mL min^{-1}	n.a.	-
[23]	Ni confined in SiO_2 nanofiber (electrospinning)	0.4	700	48	10	12	TEM	CO_2:CH_4:Ar = 1:1:2 80 mL min^{-1}	60	-
[24]	Ni nanoparticles immobilized on Ce-modified mesoporous silica	0.1	450	18	10	10	H_2 chemisorption	CO_2:CH_4 = 1:1 15 mL min^{-1}	n.a.	-
[25]	NiCo@SiO_2 core-shell	0.1	800	600	10	15	CO chemisorption	CO_2:CH_4:N_2 = 1:1:1	87	**[45]**
[26]	Ni in silica nanocapsules	9.6	700	3600	12.3	14.4	H_2 chemisorption	CO_2:CH_4 = 1:1	n.a.	**[14]**

[a] Initial (when mentioned) TOF value of the best catalyst; [b] Temperature used when TOFs were calculated; [c] Nickel dispersion; [d] CH_4 conversion for TOF calculation; [e] Reference number in the manuscript; n.a. not available.

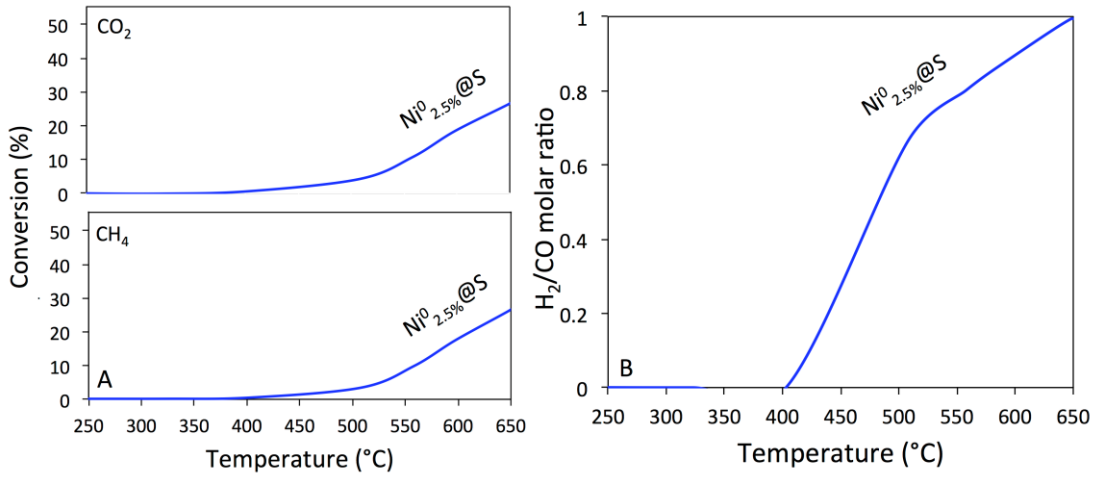

Figure S15: *A) CH_4 and CO_2 conversions and B) H_2/CO molar ratio in the DRM reaction on $Ni^0_{2.5\%}$@S as a function of temperature (GHSV of 960 L g^{-1} h^{-1}).*

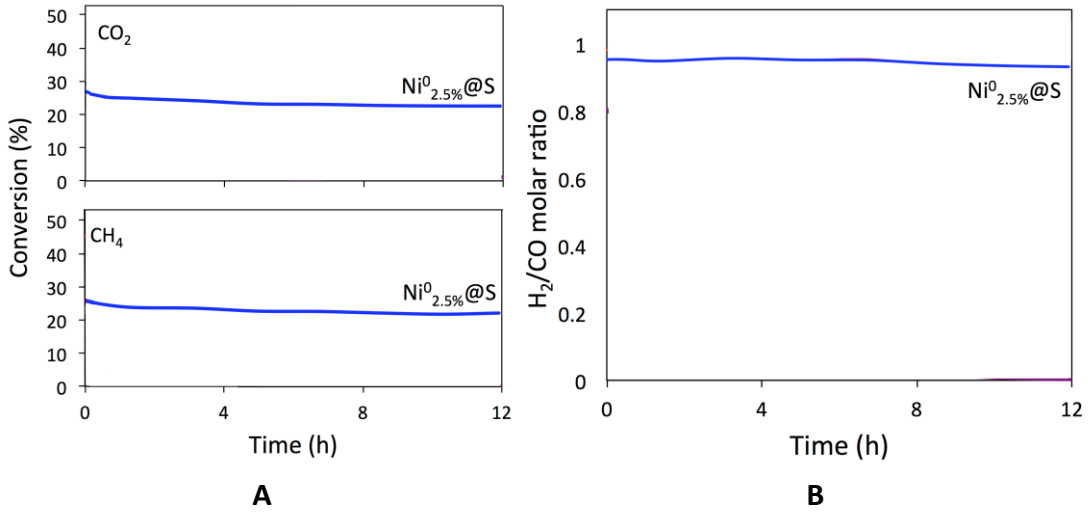

Figure S16: *A) CH_4 and CO_2 conversions and B)H_2/CO molar ratio reaction on $Ni^0_{2.5\%}$@S at 650°C for 12 h on stream under a GHSV of 960 L g^{-1} h^{-1}.*

TOF calculation in the manuscript

$$\text{TOF } (s^{-1}) = \left(\frac{\frac{0.48}{Vm} * Conversion\ \%}{\frac{Ni\ wt.\ \% * Catalyst\ wt.}{59} * Dispersion\ \%} \right) / 3600$$

Pure CH_4 flow = 0.48 L h^{-1}

Vm (molar volume) = 22.4 L mol^{-1}

M_{Ni} = 59 g mol^{-1}

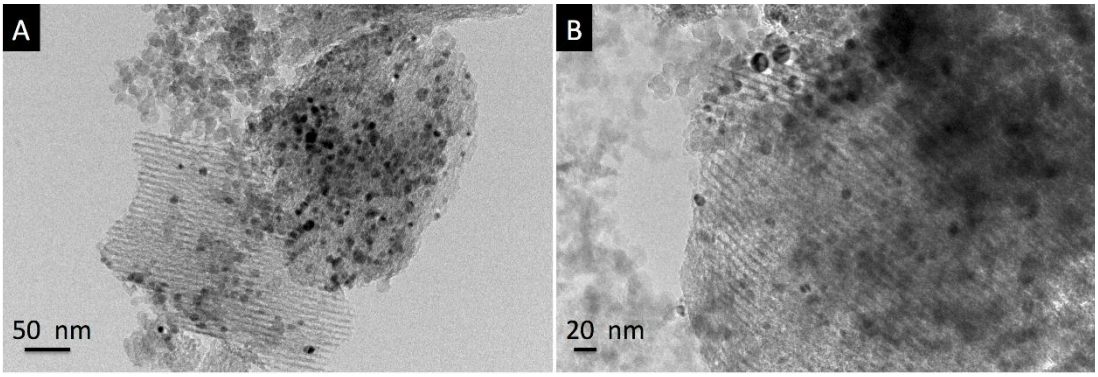

Figure S17: *A and B: Representative TEM images taken on some typical areas of spent* $Ni^{0}_{5\%}/S$.

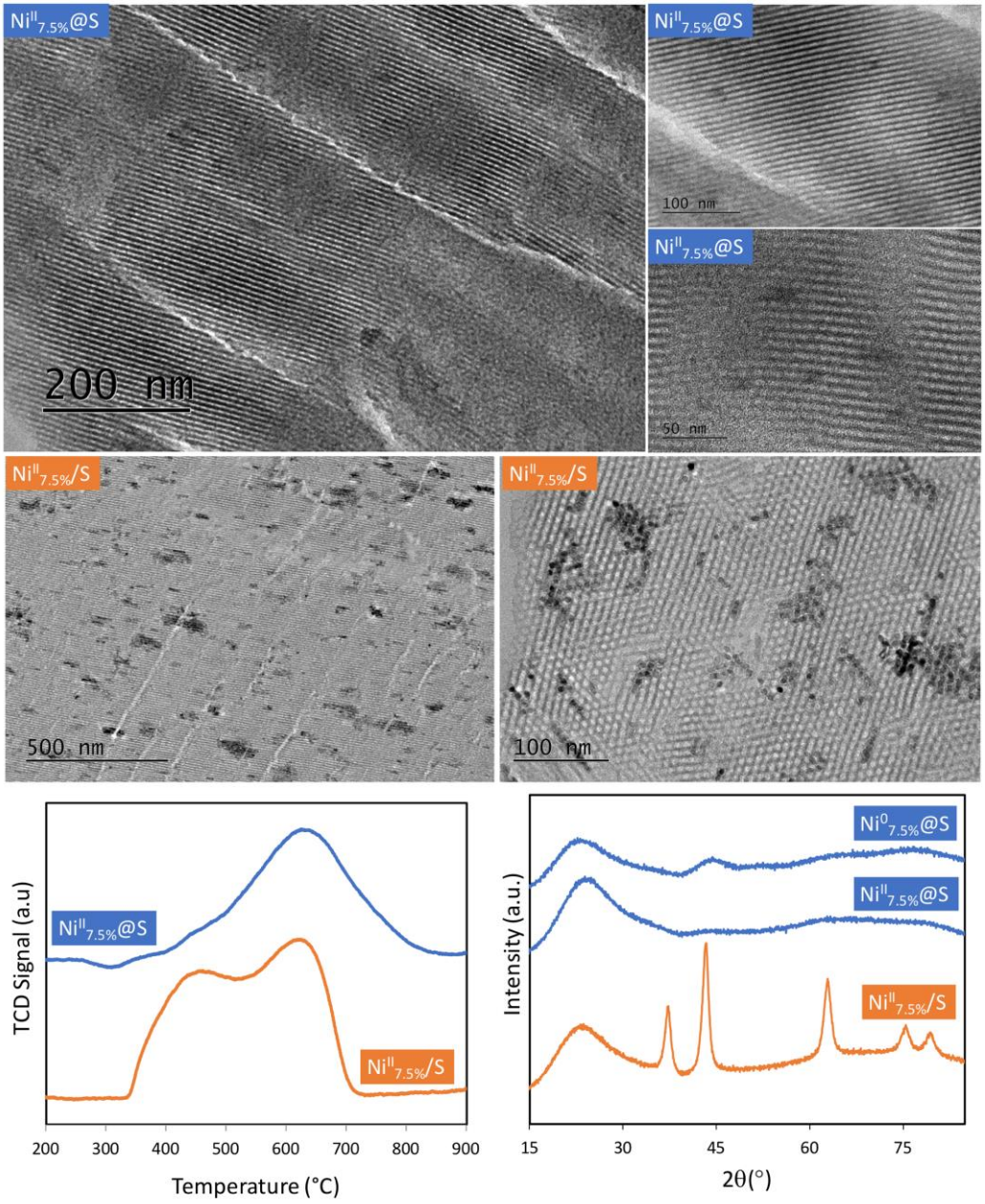

Figure S18: *Summary of relevant results of* $Ni_{7.5\%@S}$ *vs.* $Ni_{7.5\%}/S$ *including TEM images, Ni reducibility (*H_2*-TPR) as well as XRD patterns revealing the effectiveness of the one-pot preparation method while increasing the metal loading.*

References:

[1] Q. Liu,Y. Tian, One-pot synthesis of NiO/SBA-15 monolith catalyst with a three-dimensional framework for CO_2 methanation, International Journal of Hydrogen Energy, 42 (2017) 12295-12300, https://doi.org/10.1016/j.ijhydene.2017.02.070.

[2] M. E. Gálvez, A. Albarazi, P. Da Costa, Enhanced catalytic stability through non-conventional synthesis of Ni/SBA-15 for methane dry reforming at low temperatures, Appl. Catal. A: Gen. 504 (2015) 143-150, https://doi.org/10.1016/j.apcata.2014.10.026.

[3] L. Karam, S. Casale, H. El Zakhem N. El Hassan, Tuning the properties of nickel nanoparticles inside SBA-15 mesopores for enhanced stability in methane reforming, J. CO_2 Util. 17 (2017) 119-124, https://doi.org/10.1016/j.jcou.2016.12.002.

[4] M. N. Kaydouh, N. El Hassan, A. Davidson, S. Casale, H. El Zakhem, P. Massiani, Effect of the order of Ni and Ce addition in SBA-15 on the activity in dry reforming of methane, C. R. Chimie 18 (2015) 293-301, https://doi.org/10.1016/j.crci.2015.01.004.

[5] X. Gao, H. Liu, K. Hidajat, S. Kawi, Anti-Coking Ni/SiO_2 Catalyst for Dry Reforming of Methane: Role of Oleylamine/Oleic Acid Organic Pair, ChemCatChem 7 (2015) 4188-4196, https://doi.org/10.1002/cctc.201500787.

[6] H. Peng, X. Zhang, L. Zhang, C. Rao, J. Lian, W. Liu, J. Ying, G. Zhang, Z. Wang, N. Zhang, X. Wang, One-Pot Facile Fabrication of Multiple Nickel Nanoparticles Confined in Microporous Silica Giving a Multiple- Cores@Shell Structure as a Highly Efficient Catalyst for Methane Dry Reforming, ChemCatChem 9 (2017) 127-136, https://doi.org/10.1002/cctc.201601263.

[7] J. Woo Han, J. Seong Park, M. Suk Choi, H. Lee, Uncoupling the size and support effects of Ni catalysts for dry reforming of methane, Appl. Catal. B: Env. 203 (2017) 625-632, https://doi.org/10.1016/j.apcatb.2016.10.069.

[8] L. Qian, K. Huang, H. Wang, M. C. Kung, H. H. Kung, J. Li, G. Chen, Q. Du, Evaluation of the catalytic surface of Ni impregnated meso-microporous silica KIT-6 in CH_4 dry reforming by inverse gas, Microp. Mesop. Mater. 243 (2017) 301-310, https://doi.org/10.1016/j.micromeso.2016.11.029.

[9] X.Y. Gao, J. Ashok, S. Widjaja, K. Hidajat, S. Kawi, Ni/SiO_2 catalyst prepared via Ni-aliphatic amine complexation for dry reforming of methane: Effect of carbon chain number and amine concentration, Appl. Catal. A: Gen. 503 (2015) 34-42, https://doi.org/10.1016/j.apcata.2015.07.005.

[10] Z. Taherian, M. Yousefpour, M. Tajally, B. Khoshandam, Promotional effect of samarium on the activity and stability of Ni-SBA-15 catalysts in dry reforming of methane, Microp. Mesop. Mater. 251 (2017) 9-18, https://doi.org/10.1016/j.micromeso.2017.05.027.

[11] C. Wang, Y. Qiu, X. Zhang, Y. Zhang, N. Sun, Y. Zhao, Geometric design of a Ni@silica nano-capsule catalyst with superb methane dry reforming stability: enhanced confinement effect over the nickel site anchoring inside a capsule shell with an appropriate inner cavity, Catal. Sci. Technol. 8 (2018) 4877-4890,
https://doi.org/10.1039/C8CY01158C.

[12] M. Wang, Q. Zhang, T. Zhang, Y. Wang, J. Wang, K. Long, Z. Song, X. Liu, P. Ning, Facile one-pot synthesis of highly dispersed Ni nanoparticles embedded in HMS for dry reforming of methane, Chem. Eng. J. 313 (2017) 1370-1381, https://doi.org/10.1016/j.cej.2016.11.055.

[13] Z. Li, Z. Wang, B. Jiang, S. Kawi, Sintering resistant Ni nanoparticles exclusively confined within SiO_2 nanotubes for CH_4 dry reforming, Catal. Sci. Technol. 8 (2018) 3363-3371, https://doi.org/10.1039/C8CY00767E.

[14] W. Li, Z. Zhao, X. Guo, G. Wang, Employing a Nickel-Containing Supramolecular Framework as Ni Precursor for Synthesizing Robust Supported Ni Catalysts for Dry Reforming of Methane, ChemCatChem 8 (2016) 2939-2952, https://doi.org/10.1002/cctc.201600448.

[15] X. Yan, T. Hu, P. Liu, S. Li, B. Zhao, Q. Zhang, W. Jiao, S. Chen, P. Wang, J. Lu, L. Fan, X. Deng, Y.-X. Pan, Highly efficient and stable Ni/CeO_2-SiO_2 catalyst for dry reforming of methane: Effect of interfacial structure of Ni/CeO_2 on SiO_2, Appl. Catal. B: Env. 246 (2019) 221-231, https://doi.org/10.1016/j.apcatb.2019.01.070.

[16] Y. Cao, M. Lu, J. Fang, L. Shi, D. Zhang, Hexagonal boron nitride supported mesoSiO_2-confined Ni catalysts for dry reforming of methane, Chem. Commun. 53 (2017) 7549-7552, https://doi.org/10.1039/C7CC02007D.

[17] J. Zhang, F. Li, Coke-resistant Ni@SiO_2 catalyst for dry reforming of methane, Appl. Catal. B: Environ. 176-177 (2015) 513-521, https://doi.org/10.1016/j.apcatb.2015.04.039.

[18] Z. Li, S. Kawi, Multi-Ni@Ni phyllosilicate hollow sphere for CO_2reforming of CH_4: influence of Ni precursors on structure, sintering, and carbon resistance, Catal. Sci. Technol. 8 (2018) 1915-1922, https://doi.org/10.1039/C8CY00024G

[19] X. Zhao, H. Li, J. Zhang, L. Shi, D. Zhang, Design and synthesis of NiCe@m-SiO_2 yolk-shell framework catalysts with improved coke- and sintering-resistance in dry reforming of methane, Int. J. Hydrogen. Energ. 41 (2016) 2447-2456, https://doi.org/10.1016/j.ijhydene.2015.10.111.

[20] C. Chen, X. Wang, L. Zhang, X. Zou, W. Ding, X. Lu, Synthesis of mesoporous Ni-La_2O_3/SiO_2 by ploy(ethylene glycol)-assisted sol-gel route as highly efficient catalysts for dry reforming of methane with a H_2/CO ratio of unity, Catal. Commun. 94 (2017) 38-41, https://doi.org/10.1016/j.catcom.2017.02.018.

[21] W. Donphai, T. Witoon, K. Faungnawakij, M. Chareonpanich, Carbon-structure affecting catalytic carbon dioxide reforming of methane reaction over Ni-carbon composites, J. CO_2 Util. 16 (2016) 245-256, https://doi.org/10.1016/j.jcou.2016.07.011.

[22] X. Zhao, M. Lu, H. Li, J. Fang, L. Shi, D. Zhang, In situ preparation of Ni nanoparticles in cerium-modified silica aerogels for coking- and sintering-resistant dry reforming of methane, New J. Chem. 41 (2017) 4869-4878, https://doi.org/10.1039/C7NJ00115K.

[23] S. Wen, M. Liang, J. Zou, S. Wang, X. Zhu, L. Liu, Z. Wang, Synthesis of a SiO_2 nanofibre confined Ni catalyst by electrospinning for the CO_2 reforming of methane, J. Mater. Chem. A, 3 (2015) 13299-13307, https://doi.org/10.1039/C5TA01699A.

[24] T. Xie, X. Zhao, J. Zhang, L. Shi, D. Zhang, Ni nanoparticles immobilized Ce-modified mesoporous silica via a novel sublimation-deposition strategy for catalytic reforming of methane with carbon dioxide, Int. J. Hydrogen. Energ. 40 (2015) 9685-9695, https://doi.org/10.1016/j.ijhydene.2015.06.008.

[25] Y. Zhao, H. Li, H. Li, NiCo@SiO_2 core-shell catalyst with high activity and long lifetime for CO_2 conversion through DRM reaction, Nano Energ. 45 (2018) 101-108, https://doi.org/10.1016/j.nanoen.2017.12.023.

[26] C. Wang, X. Jie, Y. Qiu, Y. Zhao, H.A. Al-Megren, S. Alshihri, P.P. Edwards, T. Xiao, The importance of inner cavity space within Ni@SiO_2 nanocapsule catalysts for excellent coking resistance in the high-space-velocity dry reforming of methane, Appl. Catal. B: Env. 259 (2019) 118019, https://doi.org/10.1016/j.apcatb.2019.118019.